

# Acoustic subsurface-atomic force microscopy: Three-dimensional imaging at the nanoscale

Cite as: J. Appl. Phys. **129**, 030901 (2021); doi: [10.1063/5.0035151](https://doi.org/10.1063/5.0035151)

Submitted: 29 October 2020 · Accepted: 24 December 2020 ·

Published Online: 14 January 2021



View Online



Export Citation



CrossMark

Hossein J. Sharahi,<sup>1</sup> Mohsen Janmaleki,<sup>2</sup> Laurene Tetard,<sup>3</sup>  Seonghwan Kim,<sup>1</sup>  Hamed Sadeghian,<sup>4,5</sup>  and Gerard J. Verbiest<sup>6,a</sup> 

## AFFILIATIONS

<sup>1</sup>Department of Mechanical and Manufacturing Engineering, University of Calgary, 2500 University Dr. NW., Calgary, Alberta T2N 1N4, Canada

<sup>2</sup>Center for Bioengineering Research and Education, Biomedical Engineering Graduate Program, University of Calgary, 2500 University Dr. NW., Calgary, Alberta T2N 1N4, Canada

<sup>3</sup>NanoScience Technology Center and Department of Physics, University of Central Florida, Orlando, Florida 32816, USA

<sup>4</sup>Nearfield Instruments B.V., Rotterdam, Zuid-Holland 3047 AT, The Netherlands

<sup>5</sup>Department of Mechanical Engineering, Eindhoven University of Technology, Eindhoven, Noord-Brabant 5612 AZ, The Netherlands

<sup>6</sup>Department of Precision and Microsystems Engineering, Delft University of Technology, Mekelweg 2, 2628 CD Delft, The Netherlands

<sup>a</sup>Author to whom correspondence should be addressed: [G.J.Verbiest@tudelft.nl](mailto:G.J.Verbiest@tudelft.nl)

## ABSTRACT

The development of acoustic subsurface atomic force microscopy, which promises three-dimensional imaging with single-digit nanometer resolution by the introduction of ultrasound actuations to a conventional atomic force microscope, has come a long way since its inception in the early 1990s. Recent advances provide a quantitative understanding of the different experimentally observed contrast mechanisms, which paves the way for future applications. In this Perspective, we first review the different subsurface atomic force microscope modalities: ultrasonic force microscopy, atomic force acoustic microscopy, heterodyne force microscopy, mode-synthesizing atomic force microscopy, and near-field picosecond ultrasonic microscopy. Then, we highlight and resolve a debate existing in the literature on the importance of the chosen ultrasound excitation frequencies with respect to the resonance frequencies of the cantilever and the observed contrast mechanisms. Finally, we discuss remaining open problems in the field and motivate the importance of new actuators, near-field picosecond ultrasonics, and integration with other techniques to achieve multi-functional non-destructive three-dimensional imaging at the nanoscale.

Published under license by AIP Publishing. <https://doi.org/10.1063/5.0035151>

## I. INTRODUCTION

Advances in microscopy are driven by the desire to image objects that are invisible for the human eye. As a result, progress in nanoscale imaging and characterization of nanocomposite,<sup>1</sup> two-dimensional materials,<sup>2</sup> semiconductors,<sup>3</sup> and cell biology<sup>4,5</sup> pave the way to a deeper understanding of complexities of functional materials and systems at small scales. Despite advances reported to date, the need to visualize surface and subsurface features non-destructively at the nanoscale persists, particularly, for composites with sub-micrometer phases and for biological

systems including tissues, cells and their organelles, bacteria, and viruses. A number of applications require ultimately single-digit nanometer resolution in three dimensions (3D) using a non-destructive method (see Fig. 1). Although a wide range of microscopy techniques is available, utilizing ultrasound,<sup>6,7</sup> electrons,<sup>8</sup> photons,<sup>9,10</sup> x rays,<sup>11,12</sup> nuclear magnetic resonances,<sup>13,14</sup> and vibration spectroscopy,<sup>15–18</sup> none of these techniques achieve non-destructively single-digit nanometer resolution in 3D. A general purpose 3D imaging technique with sub-100 nm spatial resolution would revolutionize our understanding of complex systems at small scales.

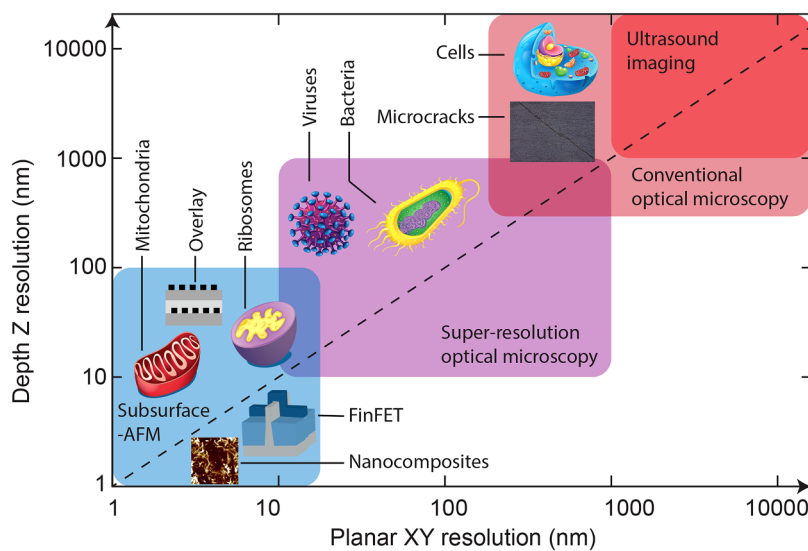


**FIG. 1.** The required 3D resolution as a function of the characteristic size of nm scale features. The applicability regimes of different techniques are indicated with colored boxes. Conventional ultrasound imaging only resolves features larger than  $1\text{ }\mu\text{m}$ . Conventional optical imaging goes down in resolution to  $200\text{ nm}$ . Super-resolution optical microscopy can resolve features in the plane with nm resolution but lacks resolution in the focus direction. Consequently, the only technique that can resolve 3D features down to the nanoscale is subsurface AFM.

Currently, one can identify three major trends in microscopy with the aim to enable 3D resolution at the nanoscale,

- super-resolution optical microscopy,
- near-field picosecond ultrasonic microscopy, and
- acoustic subsurface AFM.

Out of these trends, super-resolution optical microscopy makes use of optical tricks such as stimulated emission to obtain a resolution well below the diffraction limit in the imaging plane.<sup>19</sup> This technique only works in optically transparent samples such as cells, which limits the range of applications. Moreover, the light intensities are destructive for the samples, and the fluorescence tag can interfere with processes in the living systems in a manner that is currently not determinable.<sup>19</sup>

Nanoscale characterization in 3D can be performed in AFM using 3D force mappings or force spectroscopy. The 3D force mappings are usually slow and invasive,<sup>20,21</sup> as the AFM tip scans in a synchronized and sequential way the tip-sample interface in 3D. The force exerted by the tip is recorded for different vertical displacements to generate a 3D force map. This approach is usually slow and invasive; however, it provides 3D nanoscale information.<sup>22,23</sup> Subsurface information is possible in an AFM using thermal (scanning thermal microscopy),<sup>24</sup> electrical (Kelvin probe force microscopy),<sup>25</sup> and acoustic (ultrasonic AFM)<sup>26</sup> excitations.

Low-power acoustic waves are advantageous for non-destructive imaging as they induce minimal stress and heat on a material. The speed at which the ultrasound waves propagate is directly related to the wavelength and frequency and is specific to a material. However, the wavelength of the most common ultrasonic actuator ranges from 0.1 to 100 MHz, which corresponds to the wavelength of several micrometers and beyond. Hence, acoustic imaging is limited by diffraction and cannot readily probe nanoscale features. One approach considered to improve the spatial resolution of ultrasonic microscopy

has focused on using higher frequency waves, generated by ultrashort laser pulses. Picosecond and also femtosecond ultrasonic spectroscopy use a pump-probe scheme to detect the sample response to the ultrashort excitation (pump) and have been reported to offer nanoscale depth resolution. To reach lateral resolution with such an approach, new developments considering near-field monitoring of the sample upon excitation with the ultrashort pulse are being considered. Another approach to characterize materials with ultrasounds is to couple the acoustic actuation in the 0.1 to 100 MHz range to an AFM measurement to locally detect the sample response.

Ultrasonic force microscopy (UFM) was the first reported technique coupling ultrasonic and AFM capabilities.<sup>26</sup> In this mode, the sample is excited at ultrasonic frequencies much greater than the first resonant mode of the cantilever (typically MHz frequencies are used), using a piezoelectric actuator beneath the sample.<sup>27</sup> Greater sensitivity to deep nanoscopic and microscopic subsurface features than what can be achieved with AFM has been demonstrated when using multiple actuators such as with heterodyne force microscopy (HFM)<sup>28</sup> and mode-synthesizing atomic force microscopy (MSAFM).<sup>29</sup> All methods could provide nanoscale lateral and depth imaging, though the nature of the contrast remains difficult to assess.

Based on the limitations of existing techniques, we identify the acoustic subsurface AFM as the most promising approach to realize a general 3D non-destructive nano-acoustic imaging technique, without the need for fluorescence tag. Such a platform holds the potential to enable deep subsurface imaging of soft (biological and polymers structure) and hard materials (engineered systems). For example, UFM is used to characterize amyloid- $\beta$  peptides in protein fibers.<sup>30</sup> Moreover, HFM was applied to visualize the aggregation of carbon nanoparticles that is buried in red blood cells.<sup>31</sup> To quantitatively interpret the subsurface image, the exact contrast mechanisms of subsurface imaging should be investigated in greater detail. It has been suggested that the contrast in acoustic subsurface AFM results from different factors including contact

stiffness variations between the tip and the sample,<sup>32–35</sup> scattering of ultrasonic waves by buried nano-features,<sup>35–37</sup> and friction.<sup>38–40</sup>

In this Perspective, we will first discuss the different modalities in nano-acoustic imaging before focusing on the identified contrast mechanisms and highlight current debates in the field by discussing different excitation schemes. Next, we will discuss existing applications and limitations in nano-acoustic imaging. Finally, we will provide our view on the future direction of the field.

## II. IMAGING MODALITIES

Atomic force microscopes are used as a common surface characterization technique that can achieve nanometer spatial resolution in three dimensions. Conventional AFM techniques operating in contact or the tapping mode have shown sensitivity to shallow subsurface features.<sup>41</sup> This motivated the introduction of ultrasonic methods in an AFM to develop nondestructive techniques with the nanoscale resolution that are sensitive to both the mechanical properties of the surface and deeply buried subsurface features. In this Perspective, all schemes combining ultrasound excitations and

AFM are labeled acoustic subsurface AFM. Most of the reported implementations work in contact modes such that the deflection of the cantilever is kept constant using a feedback loop. The ultrasound vibration modulates the tip-sample contact at a frequency that is too high for the feedback loop to compensate for. The dynamic cantilever's response is used to evaluate the elasticity of samples and to detect subsurface defects. The detection and visualization of subsurface features are often difficult to determine with conventional AFM modes. The differentiation between implementations of acoustic subsurface AFM is based on the frequency range of the acoustic waves, on whether the actuations are applied to the sample, the cantilever, or both, and on the number of actuations. We categorize them in three main types: (1) ultrasonic force microscopy (UFM) and atomic force acoustic microscopy (AFAM) where an ultrasound signal is applied to either the sample or cantilever, (2) heterodyne force microscopy (HFM) where both of the sample and cantilever are excited, and (3) mode-synthesizing atomic force microscopy (MSAFM) where multiple acoustic excitations are applied on the cantilever and/or sample. A summary of these configurations is provided in Fig. 2(a).

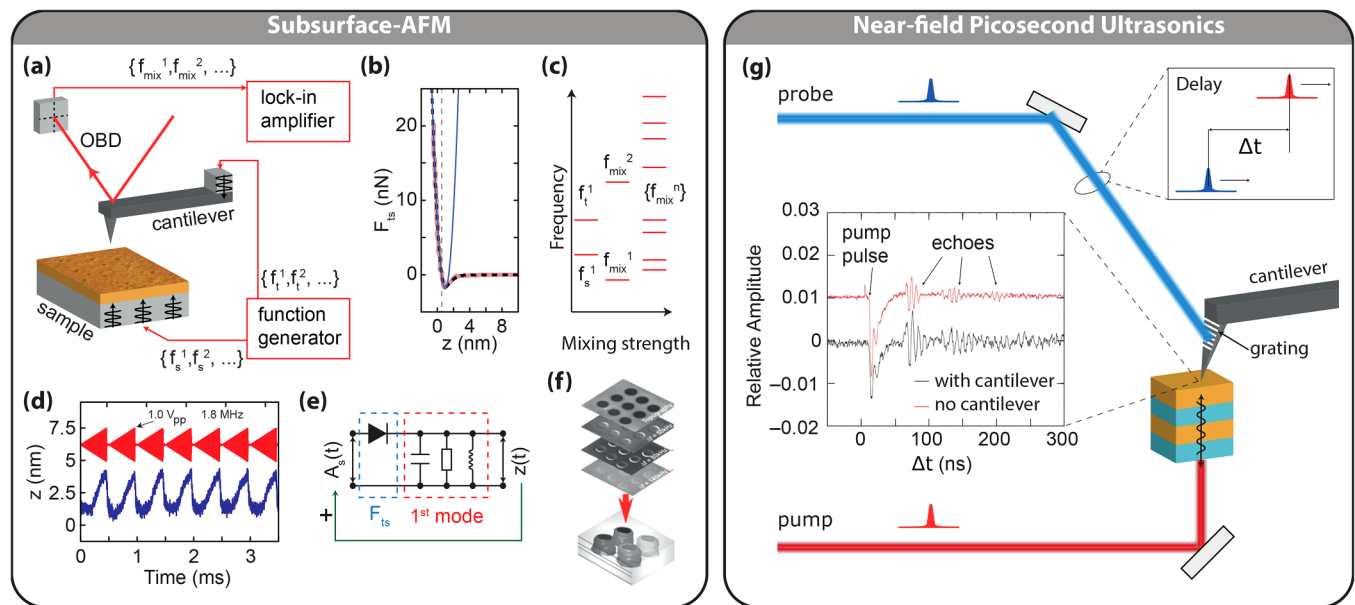


**FIG. 2.** (a) Acoustic subsurface AFM uses one or multiple ultrasound excitations of the sample (at frequencies  $\{f_s^1, f_s^2, \dots\}$ ) and/or cantilever (at frequencies  $\{f_t^1, f_t^2, \dots\}$ ) and records the cantilever motion at their mixing frequencies (at frequencies  $\{f_{mix}^1, f_{mix}^2, \dots\}$ ) using the optical beam deflection (OBD) method. These mixing frequencies are generated by the nonlinear dependence of the tip-sample force  $F_{ls}$  as a function of the tip-sample separation  $z$ , as depicted in (b) and (c). Here, the pink line is measured data and the dashed black line is the corresponding analytical model for  $F_{ls}$ . (b) To describe  $F_{ls}$  at the vertical dashed line, one needs at least a quadratic polynomial (blue line). The nonlinear  $F_{ls}$  results in nonlinear frequency mixing, hence, in many detectable  $\{f_{mix}^n\}$  with increasing mixing strength. The different modalities in the acoustic subsurface AFM owe their name to a particular choice of excitation frequencies on the sample and/or tip. (d) For example, UFM using an amplitude-modulated high-frequency excitation signal on the sample (red). The cantilever can only follow the modulation frequency, this results in a rectifying effect (blue). (e) The resulting cantilever response  $z(t)$  also modulates the tip-sample separation, similar to the ultrasound motion; hence, it couples back into the  $F_{ls}$  (green arrow), which complicates the modeling of the acoustic subsurface AFM. (f) By combining the recorded signals at different  $\{f_{mix}^1, f_{mix}^2, \dots\}$ , it is under certain conditions possible to reconstruct a 3D image of the measured device. (g) Near-field picosecond ultrasonics uses an ultrashort laser pump-probe technique in combination with a cantilever probe in order to perform pulse-echo measurements in the nanoscale (inset). By varying the delay  $\Delta t$  between the pump and probe pulse, the measurement depth can be controlled. Adapted from Refs. 38 and 42–44.

### A. Single-acoustic actuation combined with AFM

The original design of combining acoustic and AFM implemented a single ultrasound excitation [frequency  $f_i$ , amplitude  $A_i$ , where  $i$  represents whether the actuation was applied to the tip (t) or the sample (s)] and was operated in the contact mode. The techniques using sample actuations include UFM, atomic force acoustic microscopy (AFAM), and contact resonance atomic microscopy (CR-AFM). AFAM and CR-AFM employ a sinewave with a constant amplitude at a frequency near the resonance frequencies ( $f_{res}$ ) of the cantilever in contact with the sample, while UFM operates using an amplitude modulation signal well below the resonance of the cantilever. CR-AFM can also be carried out with tip actuation, which is referred to as ultrasonic atomic force microscopy (UAFM).<sup>45</sup>

In the UFM mode, the *nonlinear* tip-sample interaction  $F_{ts}$  as a function of the tip-sample distance  $z$  [see Fig. 2(b)] generates a force at the modulation frequency  $f_{mod} \ll f_s$ . Consequently, the dynamic motion of the cantilever will contain a vibration with amplitude  $A_{mod}$  and phase  $\phi_{mod}$  at the modulation frequency.

The UFM method operates in the contact mode where the deflection of the cantilever defines a certain tip-sample force  $F_{ts}$  that is to be held constant by a feedback loop. The ultrasound motion is generally of such a high frequency that it cannot be compensated for by the feedback. Therefore, the feedback loop responds to an average tip-sample force  $\langle F_{ts} \rangle$ , which is just the average force over one ultrasound cycle of duration  $T_s = 1/f_s$ ,

$$\langle F_{ts} \rangle = \frac{1}{T_s} \int_0^{T_s} F_{ts}(z_b + \delta + A_s \cos 2\pi f_s t) dt, \quad (1)$$

where  $z_b$  is the base position of the cantilever and  $\delta$  its deflection. To understand a UFM measurement, we need to consider the non-linearity of the tip-sample surface interaction forces. Figure 2(b) shows the tip-sample interaction. In the UFM, the tip is in contact with the sample surface, i.e., in the repulsive force regime. When an ultrasonic vibration is applied to the sample, the tip-sample separation is changed corresponding to the amplitude of the vibration. When the amplitude of vibration  $A_s$  is small, the tip-sample distance sweeps a linear part of the force curve. In this case, the cantilever's response remains the same as in the absence of ultrasonic vibration. However, when the amplitude of ultrasonic vibration is increased, the tip-sample separation sweeps the nonlinear part of the tip-sample interaction. In this case, the cantilever's response experiences a jump deflection that is called ultrasonic deflection or ultrasonic force. This mechanism is known as a mechanical diode, as the tip-sample interaction in a sense rectifies the ultrasound vibration.<sup>46–48</sup> The AFM feedback will respond to the average force  $\langle F_{ts} \rangle$  to keep it at its given set-point. To separate this increase in deflection from the true topography, the ultrasound amplitude is modulated. The frequency  $f_{mod}$  of this modulation is set below or on the fundamental mode of the cantilever and above the bandwidth of the AFM feedback. Generally, the modulation frequency is chosen in order of a few kHz. On the other side, the carrier frequency must be chosen sufficiently higher than the resonance frequency of the cantilever. It is more common to choose a frequency in an order of a few MHz. Figure 2(d) shows an exemplary

measurement of this detection mechanism. As  $f_{mod} \leq f_{res}$ , the motion of the cantilever is well captured by the equation of motion of a harmonic oscillator,

$$\ddot{\delta} + \frac{2\pi f_{res}}{Q_{res}} \dot{\delta} + (2\pi f_{res})^2 \delta = \frac{\langle F_{ts} \rangle}{m_{eff}}, \quad (2)$$

in which  $Q_{res}$  quantifies the quality Q-factor of the cantilever and  $m_{eff}$  is its effective mass. Equation (2) has to be solved self-consistently as both the left and right side depend on  $\delta$ . The deflection  $\delta$  acts thus as a feedback parameter for the force  $\langle F_{ts} \rangle$ , as schematically illustrated in Fig. 2(d). In this figure, the ultrasonic excitation signal is modulated in amplitude with a ramp shape in which the carrier and modulation frequencies are 1.8 MHz and 2 kHz, respectively (red signal), where the AFM cantilever response measured by a position-sensitive photodiode (PSPD) shows the measured out of plane vibration of the sample (blue signal). The repetitive jump in the normal deflection of the cantilever is a result of the amplitude modulation of mixed two excitation waves. Note that  $f_{res}$  and  $Q_{res}$  are effective resonance frequency and Q-factor of the cantilever, respectively, and also depend on  $\langle F_{ts} \rangle$  (see Sec. III B). As a result, the total deflection is separated into a static component that characterizes the height and a dynamic component that represents the ultrasound signal.

AFAM and UAFM methods also operate in the contact mode. When the AFM tip is brought into contact with the sample surface, vertical and lateral elastic forces as well as adhesion forces act between the tip and the sample. Because of this tip-sample interaction, the boundary condition at the end of the cantilever changes and consequently the resonance frequency of the cantilever.<sup>49–51</sup> The nonlinear interaction forces can be modeled considering a contact stiffness ( $k^*$ ) and contact damping ( $c$ ) only. The variation of the contact resonance frequency is approximated by a harmonic oscillator model. The first resonance frequency of the cantilever far away from the sample (free) is given by Ref. 49,

$$f_{1,free} = \frac{1}{2\pi} \sqrt{\frac{k_c}{m^*}} = \frac{1.87^2}{2\pi} \sqrt{\frac{EI}{\rho A}}, \quad (3)$$

where  $m^*$  depicts the effective mass of the cantilever and  $E$ ,  $I$ ,  $\rho$ , and  $A$  denote the Young's modulus, area moment of inertia, density, and cross section area of the cantilever, respectively. The spring constant of the cantilever,  $k_c$ , can be calculated for forces acting at the end of it as

$$k_c = \frac{3EI}{L^3} = \frac{Eb^3w}{4L^3}, \quad (4)$$

where  $L$ ,  $w$ , and  $b$  are the length, width, and thickness of the cantilever, respectively. By substituting Eq. (4) in Eq. (3), the effective mass ( $m^*$ ), can be written as

$$m^* = \frac{k_c}{(2\pi f_{1,free})^2} = \frac{3\rho L w b}{(1.87 L)^4} \approx \frac{1}{4} m. \quad (5)$$

When there is a contact between the tip and sample, a second spring constant related to contact stiffness ( $k^*$ ) is added to the spring constant of the cantilever. Then, the first contact resonance frequency can be written as

$$f_{res} = \frac{1}{2\pi} \sqrt{\frac{k^* + k_c}{m^*}}, \quad (6)$$

where  $k^*$  represents the contact stiffness between the tip and the sample. The contact stiffness can be calculated from the Hertzian model.<sup>52</sup> In the simplest case, the sample is considered as a flat surface, and the tip is considered as a sphere with a radius  $R$ . If the applied force on the tip is equal to  $F_n$ , the contact stiffness between the tip and sample is given by

$$k^* = \sqrt[3]{6E^*^2RF_n}. \quad (7)$$

Here,  $E^*$  is the effective Young's modulus of the contact, which for isotropic elastic materials is defined as

$$\frac{1}{E^*} = \frac{1 - \vartheta_t^2}{E_t} + \frac{1 - \vartheta_s^2}{E_s}, \quad (8)$$

where  $E_t$ ,  $E_s$ ,  $\vartheta_t$ , and  $\vartheta_s$  are the Young's modulus and Poisson's ratios of the tip and sample, respectively. Equations (7), and (8) depict that the contact stiffness is affected by the material properties of the sample. Considering Eq. (6) subsequently shows that contact resonance frequency depends on the mechanical properties of the sample. Therefore, AFAM and UAFM measurements can be performed in the point-by-point mode and collecting the contact resonance frequency data at the position of interest on the sample. Mapping the mechanical properties of the sample using this approach is more time consuming due to the large number of data points that should be collected. Another approach, as with UFM, the qualitative AFAM image can be acquired by collecting a single value instead of a spectrum at each pixel. In this case, the sample (in AFAM) or cantilever (in UAFM) is excited near the contact resonance frequency. Then, the amplitude or phase signal of the cantilever is detected by lock-in amplifier, which provides a particular surface and subsurface property of the material. Both the tip and sample actuators present advantages. For instance, tip actuation makes the implementation on commercial systems more straightforward as it circumvents the use of an ultrasonic sample holder. On the other hand, some differences should be considered, the main one being the fact that in a sample actuation configuration to the entire sample is excited while in the tip configuration, the excitation is more localized. Subsurface nanoscale imaging has mainly been reported using sample actuation platforms to date. The performance of the configuration with tip actuation requires further investigation.

## B. Heterodyne force microscopy

HFM uses an ultrasound excitation of the sample,  $f_s^1$ , as well as of the cantilever,  $f_t^1$ , that are commonly induced with piezoelectric actuators.<sup>53</sup> Both excitations use a single frequency slightly

offset from one another. The nonlinear tip-sample interaction  $F_{ts}$  mixes the frequencies and generates an effective driving force at their sum and difference frequencies [see Fig. 2(c)]. Similar to the modulation frequency in UFM, the difference frequency is usually chosen on or below the contact resonance of the cantilever. This motion is characterized by an amplitude  $A_{mix}$  and phase  $\phi_{mix}$ . Note that the tip-sample distance is a superposition of the sample and the cantilever vibrations, on the basis of which the nonlinear tip-sample interaction generates the difference and sum frequency signals. Although HFM may be perceived as a straightforward extension of UFM, the mechanisms of its signal generation have only recently been understood.<sup>42,54,55</sup> The complexity of HFM is that the averaged tip-sample force  $F_{ts}$ , as defined for UFM [see Eq. (1)], may not even exist. The ultrasound frequencies  $f_s$  and  $f_t$  usually have a common period on the time scale at which the measurement is performed. The theoretical framework for this process has recently been elucidated,<sup>42</sup>

$$A_{mix} e^{i\phi_{mix}} = \frac{A_s A_t}{\sqrt{A_s^2 + A_t^2}} \frac{I_2 e^{\phi_s - \phi_t}}{H^{-1}(f_{mix}) - I_1}, \quad (9)$$

where  $\phi_s$  and  $\phi_t$  are the phases of the ultrasound vibrations in the sample and cantilever tip, respectively. The transfer function of the cantilever  $H(f_{mix})$  and functions  $I_1$  and  $I_2$  related to the tip-sample interaction are given by

$$H^{-1}(f_{mix}) = (2\pi)^2 m_{eff} \left[ (f_{res}^2 - f_{mix}^2) + i \frac{f_{res} f_{mix}}{Q_{res}} \right], \quad (10)$$

$$I_1 = \frac{1}{\pi} \int_{-1}^1 \frac{\partial F_{ts}}{\partial z} \left( z_b + \delta + \sqrt{A_s^2 + A_t^2} u \right) \frac{du}{\sqrt{1-u^2}}, \quad (11)$$

$$I_2 = \frac{1}{\pi} \int_{-1}^1 \frac{\partial F_{ts}}{\partial z} \left( z_b + \delta + \sqrt{A_s^2 + A_t^2} u \right) \frac{udu}{\sqrt{1-u^2}}. \quad (12)$$

Similar to the signal generation in UFM, Eq. (9) has to be solved self-consistently with the equation for the static deflection

$$\delta = I_0/k, \quad (13)$$

where  $I_0$  is related to the tip-sample interaction through

$$I_0 = \frac{1}{\pi} \int_{-1}^1 F_{ts} \left( z_b + \delta + \sqrt{A_s^2 + A_t^2} u \right) \frac{du}{\sqrt{1-u^2}}. \quad (14)$$

The advantage of using HFM over UFM is that it provides information of the relative phase between the two ultrasound excitations. This relative phase is directly accessible through  $\phi_{mix}$ . Initially, it was argued that the amplitude of the difference frequency resolves differences in the local sample stiffness, whereas the phase indicates differences in the sample viscoelasticity and/or adhesion.<sup>28</sup> However, the origin of contrast in HFM turns out to be more complex as it depends on numerous factors, including the

size of the characteristic feature with respect to the wavelength, the tip–sample interaction, and friction (see Sec. III).

### C. Mode-synthesizing atomic force microscopy

Mode-Synthesizing Atomic Force Microscopy (MSAFM) considers the general framework of multi-frequency AFM<sup>29,56–58</sup> and the higher order coupling modes generated by the nonlinear tip–sample interaction in the presence of two or more actuations.<sup>29</sup> Although the concept described when invoking MSAFM does not impose for actuations to be ultrasonic in nature, the first report of MSAFM<sup>29</sup> demonstrated the effect with up to three ultrasonic actuations. As with HFM, MSAFM uses transducers to create each one of the single frequency excitations at the tip ( $f_t^i$  and  $A_t^i$ ) and/or underneath the sample ( $f_s^i$  and  $A_s^i$ ). The nonlinear tip–sample interaction  $\langle F_{ts} \rangle$  constitutes the mixing component leading to the formation of multiple combinations of sum and difference frequencies ( $f_{\text{mix}}^{ij}$ ,  $A_{\text{mix}}^{ij}$ ). A semi-analytical model indicated that the amplitude of the mixing is maximal in the presence of van der Waals forces.<sup>59</sup> The model, validated experimentally, also indicated that for the synthesized mode considered, namely, the difference mode, the amplitude was more sensitive to variations in the long-range van der Waals power law than to variations in the short-range repulsive power law.<sup>59</sup> This is in agreement with experimental observations that  $A_{\text{mix}}^{ij}$  varies with respect to the tip–sample distance, showing a significant increase as the distance reaches the limit at which the tip and the sample come “out of contact” in the long-range attractive regime.<sup>59</sup>

By sweeping the driving frequencies over large frequency spans (from 50 kHz to 4 MHz), including cases where  $f_s^i > f_t^i$  and  $f_s^i < f_t^i$ , it was found that  $A_{\text{mix}}^{ij}$  consistently increases as the difference between two excitations matches one of the contact resonances of the cantilever.<sup>29</sup> The results showed that though most protocols reported for HFM considered two single excitations frequencies slightly offset from each other, with the difference frequency on or below the contact resonance of the cantilever, these conditions do not constitute stringent requirements to obtain an image. However, the contrast of the images produced varies.<sup>29</sup> When considering the amplitude of the difference mode between two ultrasonic actuations in the MHz range, the signal was found to be stronger when the  $f_s^i > f_t^i$  at a driving amplitude of 2 V<sub>pp</sub>.<sup>29</sup> The sweeps also revealed the presence of resonance frequencies emanating from the sample, a feature that was later considered by Shekhawat *et al.* as a means to image subsurface variations in the sample with lateral nanoscale resolution down to 5 nm.<sup>60</sup>

Increasing the amplitude of the driving excitation was found to strengthen the nonlinearity of the interaction, leading to a high number of synthesized modes. Up to 65 synthesized modes could be experimentally observed for a system with three actuations Fig. 2(c).<sup>29</sup>  $A_{\text{mix}}^{ij}$  was affected when increasing the driving amplitudes of the actuations from 0 to 10 V<sub>pp</sub>. This is consistent with Eq. (3). However, given the level of complexity of the multi-frequency system with strong non-linearity of the tip–sample interaction, the increase in amplitude cannot be described as a simple linear function, and energy redistribution in the various modes should be considered in details.

As with HFM, signals generated in MSAFM using a phase-locked excitation scheme provide information on the phase of each mode, which can be accessed directly via lock-in amplifier measurement. As previously mentioned, although all modes synthesized with MSAFM have been shown to be operational for imaging,<sup>29</sup> the nature of the contrast in the images remains a complex question. Sample properties (local stiffness, Poisson’s ratio, surface roughness, adhesion, viscoelasticity), friction, and the dimension of the buried features with respect to the wavelength of the synthesized modes are expected to play a role in the variation of the signals. This approach has been shown to be amenable for nanoscale subsurface imaging.<sup>40,43,45,61,62</sup> However, the optimal choice of parameters to be used to control the probing depth has not yet been clearly defined. One study by Vitry *et al.*<sup>40</sup> shed some light on this process by considering that the connection between attenuation coefficients of the respective ultrasonic actuation waves and the probing depth of the difference mode. The proof of concept could be validated on calibration samples designed using nanofabrication to embed aluminum features in a silicon layer coated with nickel [see Figs. 6(g) and 6(i)]. It is important to note that the fabrication of the calibration sample for subsurface imaging at the nanoscale is in itself a substantial challenge. In this case, the collection of sequences of MSAFM phase images while maintaining one actuation frequency fixed and tuning the other to vary the difference mode frequency made it possible to reach a three-dimensional reconstruction of the subsurface features that was in good agreement with the design of the calibration sample. Though additional work is needed in this direction, reports to date suggest that MSAFM is capable of quantitative nanoscale subsurface imaging.

### D. Near-field picosecond ultrasonic microscopy

Conventional picosecond ultrasonics spectroscopy uses ultra-short laser pulses of the order of tens of femtoseconds to generate elastic waves in a sample (i.e., pump) followed by a probe pulse that detects the amplitude and arrival time of the acoustic pulses arriving back at the surface of the sample [Fig. 2(g)].

The pump pulse increases the kinetic energy of electrons in the material. Energy transfer to the phonons follows within picoseconds. Due to the extremely short excitation time, phonons can be excited over a wide frequency range, up to a few THz, which enables the formation of an acoustic pulse. The absorbed energy results in local thermoelastic expansions of the sample generating surface and bulk acoustic waves. These propagating waves are subject to reflection, refraction, scattering, and diffraction due to variations in density, elasticity, and damping. The acoustic pulses arriving back at the surface of the sample can be detected using a probe emitted with a delay of a few picoseconds after the pump. The time-resolution of picosecond spectroscopy measurements is of the order of 1 ps and can be improved.<sup>63,64</sup> The time-resolution is related to the depth probed. In silicon, for example, the acoustic pulse would travel with a speed of 8433 m/s, resulting in a penetration depth of only 4.2 nm for a 1 ps time delay. However, the lateral resolution remains restricted by the diffraction limit.<sup>65</sup>

To reach nanoscale lateral resolution, recent advances have focused on carrying out picosecond ultrasonic measurements with near-field probes, as shown in Fig. 2(g). Ahn *et al.*<sup>66</sup> reported the implementation of high-frequency ultrasound high resolution mapping on an apertureless near-field scanning optical microscope. The work demonstrated that the intensity of the probe pulse can be enhanced by coupling the light to a AFM cantilever tip. The ultrasonic wave resulting from the process could be detected by monitoring the modulation of the backscattered near-field light during a transient state of the system, as shown in Fig. 2(g). The current record yields a spatial resolution of 100 nm even in biological samples.<sup>65</sup>

Though this approach is attractive to generate pulses with frequencies such that phonon behavior can be probed, a good control of the depth probed as a function of delay between the probe and the pump, and a sturdy approach to achieve lateral resolution is required to advance the technique to the level of quantitative nanoscale subsurface imaging. In addition, we note that the ability to generate ultrasounds is dependent on the absorption of the material. Transparent samples that do not absorb the ultrashort laser pulses cannot be studied unless special transducers are developed.

### III. CONTRAST MECHANISMS

Each nonlinear frequency component in the motion of the cantilever, characterized by the amplitude  $A_{\text{mix}}^i$  and phase  $\phi_{\text{mix}}^i$ , can be measured as a function of position. A nano-acoustic image can be reconstructed for each of these components. The contrast is then simply defined as the signal with respect to the background, i.e., measured signal when not over a subsurface feature, in the same image. For the amplitude, this yields

$$C_A = (A_{\text{mix}}^i - A_{\text{mix,b}}^i) / A_{\text{mix,b}}^i \quad (15)$$

and for the phase,

$$C_\phi = \phi_{\text{mix}}^i - \phi_{\text{mix,b}}^i, \quad (16)$$

where  $A_{\text{mix,b}}^i$  and  $\phi_{\text{mix,b}}^i$  quantify the background signal.

The contrast observed in current nano-acoustic imaging can originate from three different physical sources (see overview in Fig. 3). First, the ultrasound waves present in the sample interact with its internal structure, resulting in a position-dependent amplitude and phase of the ultrasound wave on the sample's surface. Second, the interaction between the tip of the cantilever and the sample can be position dependent. Consequently, the response of the cantilever to the ultrasound in the sample becomes position dependent resulting in an observable contrast. These spatial variations in the interaction can be due to the surface's topography but also to physical variations in the (visco-)elasticity of the sample. The latter can be the result of the internal structure of the sample. Finally, friction at the interface between tip and sample, at interfaces within the sample, and internal friction can lead to an observable contrast, as depicted in Fig. 3.

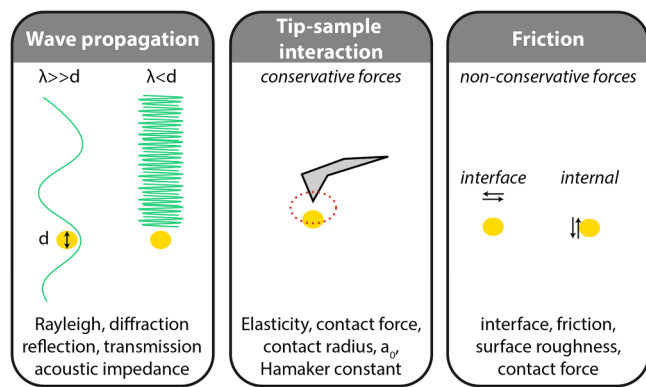


**FIG. 3.** Overview of the reported contrast mechanisms in the acoustic subsurface AFM. The left panel depicts contrast due to the wave propagation effect in the case when the ultrasound wavelength  $\lambda$  is much larger or smaller than the typical size  $d$  of the buried features. The center panel illustrates contrasts due to variations in the conservative tip-sample interaction, i.e., a change in the stress field between the cantilever and buried feature. The right panel depicts contrasts due to friction, i.e., variations in the non-conservative part of the tip-sample interaction occurring at boundaries between different materials. Each panel contains keywords for the respective contrast mechanisms.

#### A. Wave propagation

The propagation of ultrasound waves in a material can experience reflection, diffraction, scattering, and refraction. To which extent these effects are present when exciting a sample largely depends on the ultrasound wavelength and the properties of the sample. Given the speed of sound in polymers (2000 m/s), gold (3240 m/s), and silicon (8433 m/s), one can estimate the wavelength used in the acoustic subsurface AFM with actuators varying from 0.1 to 100 MHz to range between 20  $\mu\text{m}$  and 8 cm. Given that these wavelengths are at least 100 times larger than the typical features probed in the sample (and often even larger than the total sample thickness), the origin of the reported sensitivity should be carefully considered. On the other hand, efforts to carry out the measurements with higher frequency have been reported. In fact, new ultra-high frequency piezoelectric sample transducers with frequency up to 1 GHz, i.e., the wavelength of the order of 1  $\mu\text{m}$ , make it possible to reach a regime in which the wavelength of the probing wave is smaller than the dimension of the characteristic feature of the sample. Beyond 1 GHz, optically-driven processes such as in picosecond ultrasonic should be invoked. These two aspects are described further in the remainder of this section.

Let us first focus on the situation for which the ultrasound wavelength is much larger than the typical size of the features in the sample. In this particular case, the distance between the features in the sample and the AFM tip is usually much smaller than the wavelength. These measurements are thus in the so-called near-field regime. The physical contrast mechanism originates from the scattering of ultrasound waves in the sample. This scattering problem has been solved analytically for plane waves impinging on a spherical particle in the late 1950s and early 1960s of the last century.<sup>68–70</sup> Recent works have implemented these analytical calculations in

samples of finite size using finite element analysis (FEA) as shown in Figs. 4(a) and 4(b). The typical Rayleigh dependencies of the contrasts on the elastic constants (linear), the density difference between the bulk and the scattering particle (linear), on the radius  $r$  of the spherical particle [ $r^3$ , see Fig. 4(a)], and with some restrictions, on the frequency  $f_s$  of the external incoming wave ( $f_s^2$ ) have been confirmed. The depth  $d$  at which the sphere was buried seems to have little to no effect on the observed contrasts. The reason being the many reflections of the ultrasound wave between the top and bottom surface of the sample before the wave damps out. This smears out the expected analytical  $1/d$ -dependence of the contrasts completely depending on the boundary conditions [see Figs. 4(a) and 4(b)]. Using the FEA, it has been shown that  $C_A$  for a gold particle with a diameter of 20 nm in a polymer matrix under a 3 MHz excitation is of the order of  $10^{-4}$  that  $C_\phi$  is of the order of  $10^{-3}$  degrees. These contrasts are so small that it is questionable if these can ever be detected.

Now, we consider the case for which the ultrasound wavelength is smaller than or roughly equal to the typical size of the features in the sample. In this case, wave phenomena such as diffraction, reflection, and transmission determine the ultrasound propagation. The reflection and transmission of ultrasound waves at a material interface is well described by the acoustic impedance. Moreover, the differences in speed of sounds of materials

generate a time delay for the ultrasound waves arriving at the surface of a sample. Recently, the required ultrasound frequencies ( $\approx 3$  GHz) for this regime have been reached in acoustic subsurface AFM experiments using special piezoelectric transducers.<sup>67,72</sup> Hu *et al.* showed that the time delay expected based on the differences in speed of sound indeed results in the measured phase contrast<sup>67</sup> [see Figs. 4(c)–4(e)]. By using short acoustic pulses, van Neer *et al.* showed that the time delay itself can be used to quantitatively determine nanometer layer thicknesses.<sup>73</sup> The contrast in these experiments is identical to that observed in picosecond ultrasonics [see Figs. 4(f) and 4(g)]. However, one of the hurdles for picosecond ultrasonics is the imperfect contact between different materials at the nanoscale. The theory for computing the transmission and reflection of acoustic pulses using the acoustic impedance assumes a perfect contact.<sup>71</sup> In reality, however, there will be a finite interface stiffness connecting the materials that originate from the adhesion force and the interface roughness.<sup>74–76</sup> Depending on the interface stiffness value, this gives rise to a significant correction to the acoustic transmission and may possibly be reduced to zero completely. The effects of adhesion and finite interface roughness will become increasingly important for shorter acoustic pulses. Picosecond ultrasonics has just started to touch upon these topics experimentally and those results may be linked to the results in the acoustic subsurface AFM with GHz transducers.

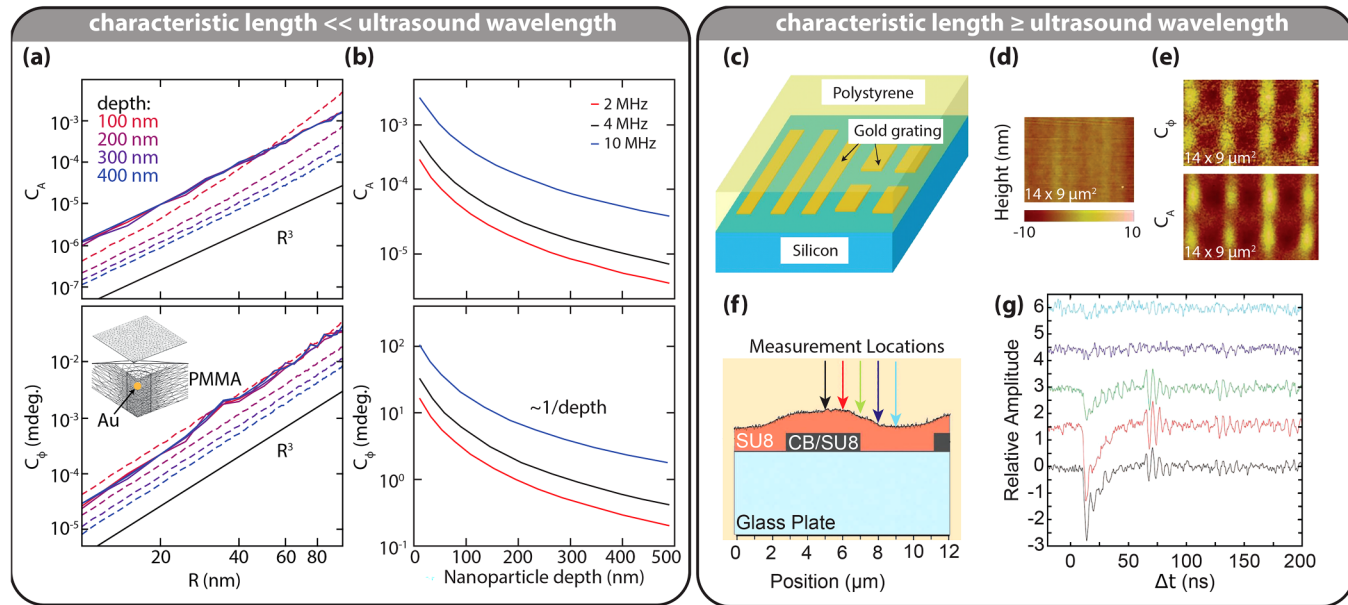


**FIG. 4.** (a) Computed amplitude and phase contrasts,  $C_A$  and  $C_\phi$ , respectively, as a function of the radius  $R$  of a buried gold nanoparticle in PMMA at a ultrasound frequency of 3 MHz. Different colors indicate different depths. The dashed lines are analytical calculations, and the continuous lines are from finite element modeling. (b)  $C_A$  and  $C_\phi$  as a function of the nanoparticle depth for an ultrasound frequency of 2 (red), 4 (black), and 10 MHz (blue). Panels (c)–(e) highlight an acoustic subsurface AFM experiment at an ultrasound frequency of 1 GHz by Hu *et al.*<sup>67</sup> (c) Gold structures deposited on silicon were covered by 200 nm thick polystyrene, which was spin-casted into the gold grating. Measured (d) topography and (e) contrasts  $C_A$  and  $C_\phi$  clearly reveal the buried gold structures. Panels (f) and (g) illustrate the near-field picosecond ultrasonics experiment by Ahn *et al.*<sup>44</sup> By measuring at different surface locations indicated in (f), the location of the buried CB/SU<sub>8</sub> composite could be detected by (g) looking at the returning ultrasound echoes. Panels adapted from Refs. 35, 36, 44, and 67.

## B. Tip-sample interaction

Current acoustic subsurface AFM techniques rely on the non-linear tip-sample interaction  $F_{ts}$  for the detection of the ultrasound. Consequently, any change in  $F_{ts}$  will affect the measured ultrasound signal.<sup>35</sup> The detection schemes for UFM, HFM, and MSAFM (see Sec. II) all rely on  $F_{ts}$  in two ways. First, a change in the tip-sample interaction itself will alter the measured signal, as can be inferred from Eqs. (1), (11), (12), and (14). Second, the tip-sample interaction will change the resonance frequencies and corresponding Q-factors of the cantilever itself. Hence, the transfer function  $H^{-1}(f_{mix})$  of the cantilever changes the detected signal (see Sec. IV). In the following, we describe known origins for variations in  $F_{ts}$  as cause for contrast in the acoustic subsurface AFM.

The tip-sample interaction arises from the contact, the separation  $z$ , and the deformation of two solid objects. Here, the solid objects are the cantilever's tip and the sample. The former is usually taken as a sphere and the latter as an infinitely large sample with a flat surface. This problem has been widely studied in the field of contact mechanics<sup>52</sup> and gave rise to the Hertz,<sup>77</sup> Lennard-Jones,<sup>78</sup> Derjaguin–Muller–Toporov,<sup>79</sup> Johnson–Kendall–Roberts,<sup>80</sup> and the Maugis–Dugdale<sup>81</sup> model. All these different models have their own range of applicability.<sup>52</sup> However, they all are parameterized by the effective elasticity  $E$  of the tip and the sample contact, the tip radius  $R$ , the Hamaker constant  $H_c$ , and a distance  $a_0$  that defines the  $z$  value of the maximal attractive tip-sample force. Any variation in these parameters can thus locally alter  $F_{ts}$ , hence, the observed contrast.

The variations in the contact radius, partly set by the tip radius  $R$ , are of less importance in the contact mode. The tip is continuously touching and indenting the sample resulting in a more or less

constant contact area. The small variations will only give rise to a smooth background in the observed subsurface contrasts.

Let us continue with the Hamaker constant  $H_c$  and the distance  $a_0$ . These parameters together with  $R$  determine the attractive part of the tip-sample interaction. Although subsurface AFM is usually operated in the contact mode, hence  $\langle F_{ts} \rangle$  is repulsive, the ultrasound vibration can cover part of the attractive regime of  $F_{ts}$ . If this happens, the cantilever comes loose from the surface for part of the ultrasound vibration, which enhances the detected signal.<sup>26</sup> Once the cantilever is probing the attractive part of  $F_{ts}$ , any change in  $H_c$  and  $a_0$  due to local changes in the sample will affect the detected signal inducing an apparent contrast in  $A_{mix}$  and  $\phi_{mix}$ . As  $H_c$  and  $a_0$  are surface properties, this contrast is not expected to be linked to (deeply) buried subsurface structures.

The main parameter determining  $F_{ts}$  in the contact mode is the effective elasticity  $E$ . The effective elasticity of the sample at its surface is a direct function of what is underneath. Several works have investigated this effect numerically for nanoparticles inside a polymer matrix.<sup>32,34,35</sup> In particular, Sharahi *et al.*<sup>35</sup> performed a FEA and found that the effective elasticity  $E$  and thus contact stiffness contrast depends on the nanoscale feature depth, size, applied force, and ultrasonic excitation frequency [see Fig. 5(b)]. It shows that the contact stiffness contrast decreases as the depth of embedded features increases. At the same depth, the contact stiffness contrast increases when the applied force on tip increases. This is mainly because of the increasing tip-sample contact area and propagation of the stress field. Figure 5(c) represents the contact stiffness contrast as a function of applied force. A gold particle, carbon nano-horns (CNHs), and a spherical cavity with a radius of 50 nm are embedded 60 nm deep in a PS matrix. In these finite element analysis, the CNHs generate greater contact stiffness contrast compare to

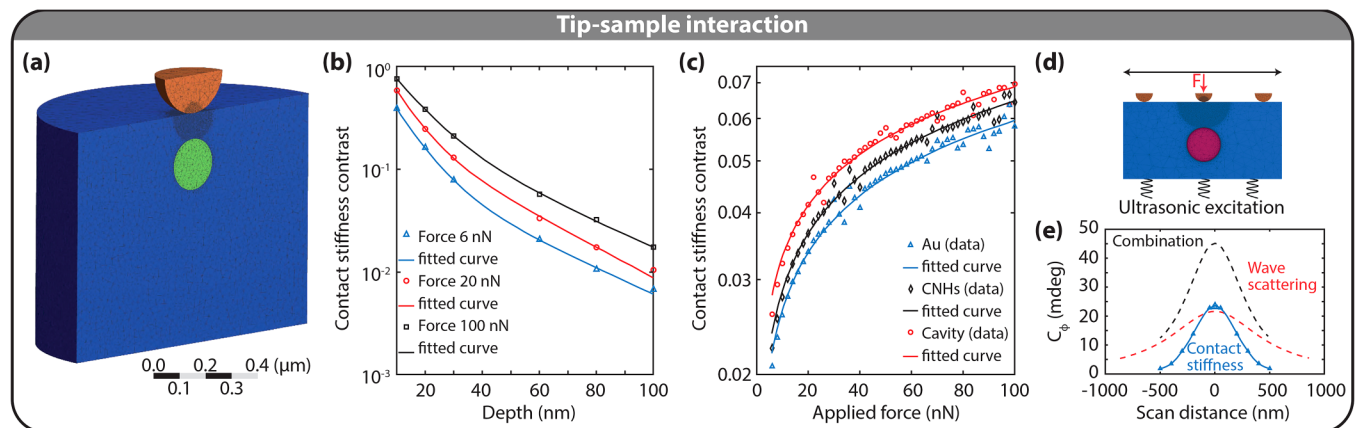


**FIG. 5.** (a) Cross section of 3D finite element mesh of a polystyrene matrix (blue), an embedded nanoparticle with a radius of 50 nm (green), and an AFM tip (orange) for the analysis of contact stiffness in acoustic subsurface imaging. The AFM tip was modeled as a hemisphere with a radius of 150 nm. (b) The contact stiffness contrast as a function of gold nanoparticle depth for three different applied forces on the tip:  $F = 6$  nN (blue triangles), 20 nN (red circles), and 100 nN (black squares). (c) The contact stiffness contrast as a function of the applied force. The gold nanoparticle, CNHs, and spherical nano-cavity have the same radius of 50 nm which are embedded 60 nm deep in a polystyrene matrix. (d) By placing the tip at different positions on the sample, the spatial extent of the contrast can be determined. (e)  $C_\phi$  from the analytical solution for Rayleigh wave scattering (red dotted line) and the contact stiffness simulation (blue data points). A Gaussian fit to the FEA data points (blue solid line) allows for the combination of the two contrast mechanisms for a total phase contrast (black dashed line). The peak contrast when the tip is directly over the nano-cavity is 45 mdeg. Panels adapted from Ref. 35.

the gold with the same applied force. The better contrast can be discussed by considering the higher values in the elastic modulus of the CNHs. Additionally, CNHs with the same dimensions at the same depth are expected to be easier to image than a comparably sized gold nanoparticle. It should be noted that the relation between the contact stiffness contrast and elastic modulus is nonlinear, and the nano-cavity gives the maximum phase contrast.<sup>35</sup>

The frequency dependence of the contrasts originates from the frequency dependent elasticity of many polymers. The depth and size can be understood naïvely by regarding the sample as three springs in series for the location of the nanoparticle and a single spring otherwise. If the materials are known, this possibly allows for the non-destructive evaluation of the nanoparticle depth using the extracted effective elasticity for different ultrasound frequencies. This idea is supported by the work of Kimura *et al.* which showed that the experimentally observed contrast indeed depends on the depth of the nanoparticle.<sup>82</sup> However, the exact relation between the subsurface feature depth and the experimentally observed contrast remains unclear. Sarioglu *et al.* showed that the stress field induced by the tip falls off rapidly with the depth into the sample.<sup>83</sup> The contact stiffness approaches the intrinsic sample material without subsurface features within 100 nm. Hence, it is unclear how small features that are buried deeper than this depth

can give a measurable contrast in experiments.<sup>82,84</sup> This is particularly difficult to understand when the feature size is smaller than the depth at which they are buried. Recent work showed that this problem is nonlinear and depends on the stress field induced by the tip, the tip shape, geometry, and material properties of the subsurface.<sup>85</sup> Moreover, it was suggested that a relation between resolution and depth can only be obtained on a case by case basis and that it is possible to detect features buried deeper than their size. To test the theory, it should be applied to experiments reported in the literature to see if it can explain the measured contrasts.

### C. Friction

In Secs. III A and III B, we were mainly concerned with *conservative* forces. In reality, the ultrasound vibrations in the subsurface AFM will dissipate energy due to friction at various instances. The observed mechanisms in the literature can be separated as (i) friction at interfaces and (ii) internal friction.

Let us start with the friction at interfaces. In the acoustic subsurface AFM, the cantilever deflection  $\delta$  depends on the present ultrasound excitations.<sup>38</sup>  $\delta$  increases with increasing ultrasound amplitudes due to the nonlinear tip-sample interaction [see Sec. II and Fig. 6(a)]. Interestingly, this heavily reduces the time that the tip is in contact with a sample, similar to conventional tapping

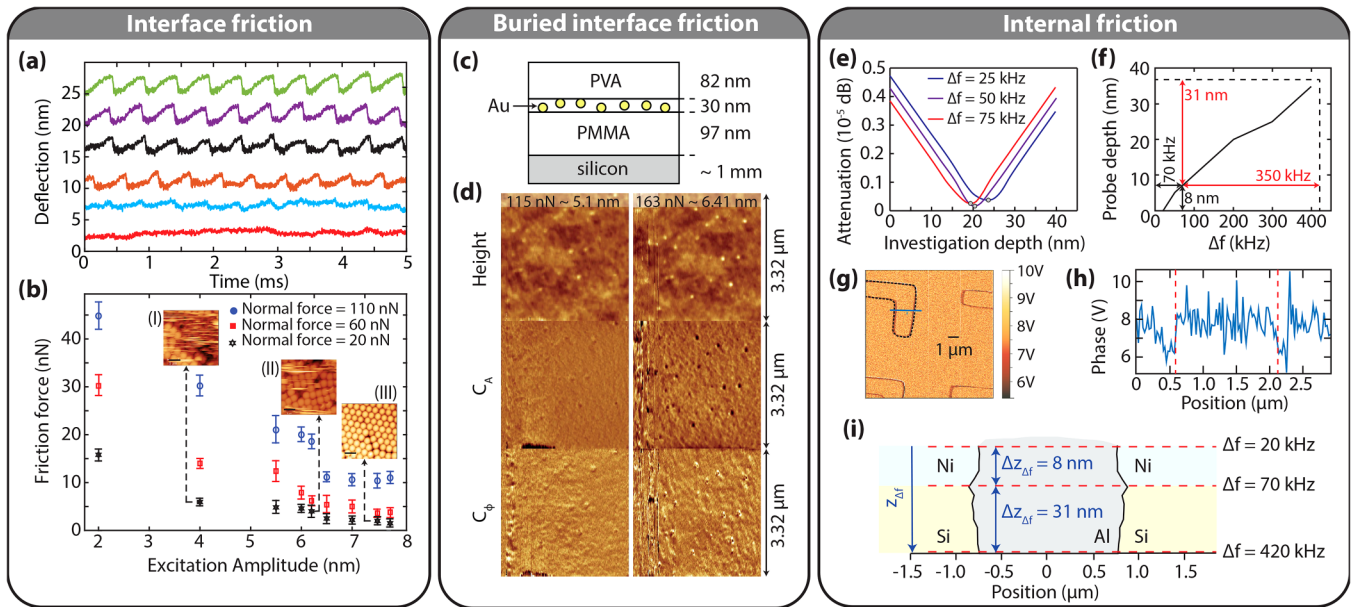


**FIG. 6.** (a) and (b) Surface friction in UFM as measured by Sharahi *et al.*<sup>38</sup> (a) Cantilever deflection signal for ultrasound excitation amplitudes increasing from 2 nm (red) to 7 nm (green) in steps of 1 nm under a load of 60 nN. For clarity, the deflection signals have been offset from one another. (b) Extracted friction force vs mean excitation amplitude while exciting the sample using the UFM mode for a constant average normal force of 20 nN, 60 nN and 110 nN. Insets labeled (I), (II), (III) show the AFM topography images of PS beads at three different amplitudes. The lateral scale bar in all AFM images is 1 μm. (c) and (d) Buried interface friction as measured by Verbiest *et al.*<sup>39</sup> (c) Schematic cross section of the measured sample. (d) HFM measurements for different contact forces: from top to bottom measured simultaneously: height,  $C_A$ , and  $C_{\phi}$  of the difference frequency. The contact force  $\langle F_{ts} \rangle$  as well as the resulting average indentation into the sample is indicated at the top in the height images. (e) and (f) Internal friction as analyzed by Vitry *et al.*<sup>40</sup> (e) Evolution of the attenuation coefficient for different  $\Delta f$ , which controls the investigation depth. (f) Representation of the dependence of relative depth of investigation  $\Delta z_{\Delta f}$  as a function of  $\Delta f$ . (g)  $C_{\phi}$  image recorded in MSAFM at  $\Delta f = 70$  kHz. The cross section at the blue line is shown in (h) and allows to extract the width of the trench. (i) By recording images at different  $\Delta f$ , a 3D reconstruction of the trench can be obtained. Panels adapted from Refs. 38–40.

mode AFM. As the average tip-sample force  $\langle F_{ts} \rangle$  increases, the induced motion of the cantilever ensures that the tip spends only a limited amount of time in contact. Although there is still a mechanical contact, damage to the sample surface is lessened as the contact is intermittent and less lateral frictional force is applied to the sample [see Fig. 6(b)]. Exactly this effect has been reported for the various modes of acoustic subsurface AFM. Variations in contact time, for example, due to changes in  $\langle F_{ts} \rangle$  or due to the sample topography may lead to changes in the lateral frictional force leading to an observable contrast.

The other interface at which friction effects occur are boundaries between different materials within the sample. Friction at these interfaces can locally reduce the ultrasound vibration amplitudes  $A_s^i$  of the sample. In HFM, it has been shown that this leads to an observable contrast in  $A_{mix}$  and  $\phi_{mix}$ . Verbiest *et al.* measured nanoparticles with a diameter of 20 nm that were buried 82 nm deep in a polymer matrix [Fig. 6(c)]. Figure 6(d) shows the measured contrast in height,  $A_{mix}$ , and  $\phi_{mix}$ , from which an energy loss of 2.79 eV per ultrasound oscillation at the buried gold nanoparticles was extracted. The observed energy dissipation nicely compares to the dissipation observed in atomic scale friction experiments, in which a sharp tip is laterally moved in contact with a surface. Moreover, the lateral size of the nanoparticles in the measured  $A_{mix}$  and  $\phi_{mix}$  contrasts was approximately equal to the buried depth. This highlights that the propagation in amplitude reduction obeys a scattering-like behavior (see Sec. III A). Dissipation at interfaces is thus a major contributor to the contrast in acoustic subsurface AFM.

We now consider internal friction, which is the ultrasound dissipation within a single material. Vitry *et al.* considered a HFM measurement scheme, in which one ultrasound wave was launched from the tip into the sample and one wave from underneath the sample.<sup>40</sup> These waves have amplitudes  $A_t$  and  $A_s$ . Once they propagate through the sample, their vibration amplitude will decrease due to the internal friction. This process is generally described by the two frequency-dependent attenuation coefficients  $\alpha_t$  and  $\alpha_s$  for the waves launched from tip and sample, respectively,

$$A_{s(t)}(z) = A_{s(t)} e^{-\alpha_{s(t)} z/v}, \quad (17)$$

where  $v$  is the velocity of ultrasonic waves in the material and  $z$  is the position into the sample with respect to where the ultrasound was launched. Within this model, the detected signal  $A_{mix}$  was considered to be proportional to  $A_s(z)A_t(z)$  [see Eq. (9)]. This results in the smallest attenuation of  $A_{mix} \propto A_s A_t e^{-(\alpha_t - \alpha_s)z/v}$  at a particular depth  $z$  [see Fig. 6(e)]. As the depth of the smallest attenuation depends on the ultrasound frequencies, the internal friction allows one to probe the subsurface structures at a particular depth as illustrated in Fig. 6(f). Using a well-defined sample [Fig. 6(g)], this method has been used to extract the width [Fig. 6(h)] of an aluminum filled trench as a function depth [Fig. 6(i)]. As friction occurs at well-defined positions within a sample, this provides a promising route toward a general 3D imaging technique at the nanoscale. MSAFM, in which multiple ultrasound waves are launched from both the tip and the sample may give access to different depths simultaneously.

#### IV. EXCITATION SCHEMES

The many different contrast mechanisms and the fact that they all occur simultaneously makes it hard to perform quantitative subsurface AFM measurements. To get insight into the exact contrast mechanism, a good understanding of the generated signal in acoustic subsurface AFM is necessary. Although it is clear that the nonlinear tip-sample interaction generates this signal at some frequency  $f_{mix}$ , the mechanical response of the cantilever itself is equally important for the signal generation. For example, choosing excitation frequencies on a contact resonance of the cantilever with high amplitudes leads to mode coupling and even chaos.<sup>88</sup> Following Eqs. (1) and (2), we see that the cantilever deflection  $\delta$  also plays a role in  $\langle F_{ts} \rangle$ . Consequently, the response of the cantilever at  $f_{mix}$ , which is set by its frequency-dependent transfer function  $H(f_{mix})$  has a back-action on the signal generation.<sup>42</sup> Moreover,  $H(f_{mix})$  itself is a function of the tip-sample interaction.<sup>87</sup> There is a debate in the literature on how and if a particular choice of excitation frequencies sets the observed contrast mechanism. In the following, we will link the different experimentally observed contrast mechanisms to particular excitation schemes.

The influence  $H(f)$  is also observed in the usual intermittent contact operation of an AFM, which is also known as a tapping mode or amplitude modulation. Here, the amplitude (or phase) of a single cantilever excitation close to a resonance peak is used to measure the topography of the surface. For this mode of operation, it is well known that variations in the elasticity of the surface influence the measured topography. The reason is that for a soft sample, a larger indentation of the sample is necessary to achieve the same force on the cantilever in comparison with a hard sample. It is this force, which is called the contact force, that determines the amplitude reduction of the cantilever's excitation. The exact amount of amplitude reduction is related to the shift in resonance frequency of the cantilever.

In addition to the response of the cantilever at  $f_{mix}$ , the ultrasound vibrations  $A_s^i$  and  $A_t^j$  themselves are dependent on the  $H(f)$ . Usually, a constant driving force on the cantilever generates the signal  $A_t^j$ . The amplitude  $A_t^j$  is solely determined by  $H(f_t)$  and thus depends on the frequency  $f_t$  and indirectly on the tip-sample interaction. A similar argument holds for the ultrasound vibrations  $A_s^i$  of the sample except that the transfer function of the sample takes on the role of  $H^{-1}(f)$ . The latter was observed by Tetard *et al.* experimentally as an increase in the amplitude of the signal at  $f_{mix}$ .<sup>59</sup>

In order to understand the different observed experimental contrasts, it is thus of utmost importance to not just know  $\{f_s^i\}$ ,  $\{f_t^j\}$ , and  $\{f_{mix}^{ij}\}$  but also all the resonance frequencies of the cantilever [see Fig. 7(a)]. Note that the resonance frequencies are a function of the tip-sample interaction [see Figs. 7(b)–7(d)]. When the tip is in contact with the sample, these frequencies are the so-called contact resonances. Depending on the choice of frequencies, the measured amplitudes  $A_{mix}^{ij}$  can be different. Hence, the observed contrast can be different. We will highlight this dependence on the example of (i) a HFM experiment in which  $\{f_s\}$ ,  $\{f_t\}$ , and  $\{f_{mix}\}$  were not matching any resonances of the cantilever and (ii) a UFM experiment in which  $f_{mix}$  was set to a contact resonance.

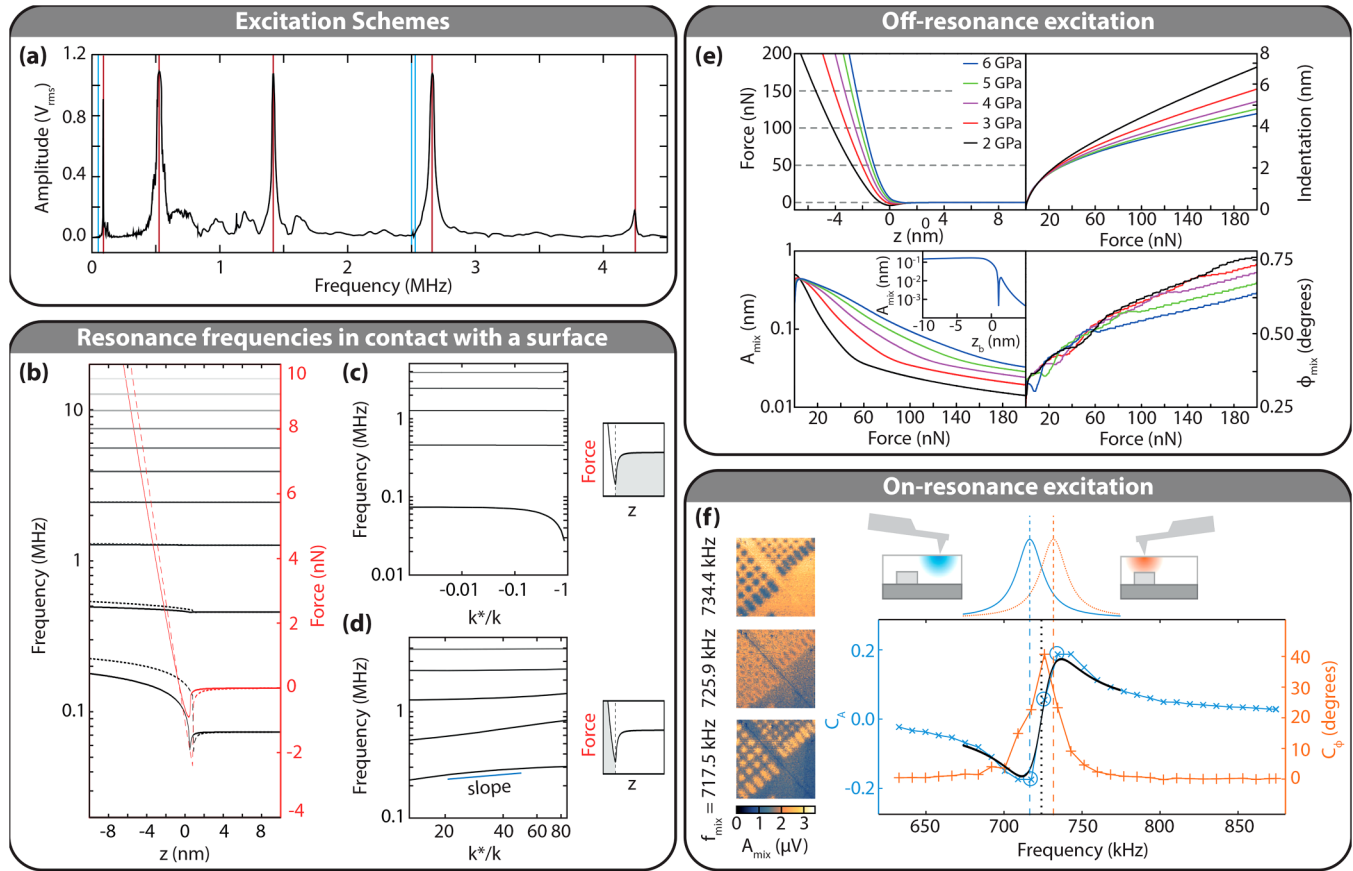


**FIG. 7.** (a) The typical vibration spectrum of a free cantilever. The red lines indicate the resonances, and the blue lines the particular excitation scheme used by Verbiest *et al.*<sup>39</sup> (b) The first 10 resonances of a cantilever as a function of the position of the cantilever's base  $z$  when the fourth mode is vibrating with an amplitude of 10 nm (continuous line) and 1 nm (dashed line). The external force  $\langle F_{ls} \rangle$  is shown in red. The first 10 resonances of the cantilever as a function of the normalized tip-sample spring  $k^*/k$  for (c) an attractive and (d) repulsive  $F_{ls}$ . The shifts of the resonance frequencies reduce for the higher modes, as these modes get stiffer with increasing resonance frequency. (e) The calculated tip-sample interaction and, as a function of the applied contact force, the corresponding sample indentation as well as the amplitude  $A_c$  and phase  $C_\phi$  of the heterodyne signal for different sample elasticities: 2 GPa (black), 3 GPa (red), 4 GPa (magenta), 5 GPa (green), and 6 GPa (blue) for the excitation scheme depicted in panel (a). The inset in the lower left panel shows  $A_c$  for 6 GPa plotted as a function of the position of the cantilever's base  $z_b$ . (f) The images on the left show the measured demodulated amplitude of the cantilever deflection at different  $f_{mix}$ . By measuring  $C_A$  and  $C_\phi$  for the 32 different images, van Es *et al.*<sup>86</sup> showed the effect of detuning between  $f_{mix}$  and the cantilever's resonance frequencies "on" and "off" the subsurface features. The data from the images on the left are marked with circles. The black line is the theoretically expected curve for the used experimental settings. Panels adapted from Refs. 39, 86, and 87.

In recent work, Verbiest *et al.*<sup>39</sup> chose all ultrasonic frequencies  $f_s = 2.52$  MHz and  $f_i = 2.50$  MHz as well as the mixing frequency  $f_{mix} = 20$  kHz not to match any resonance frequency of the cantilever [see Fig. 7(a)]. The sample used is depicted in Fig. 6(c). The authors observed a significant decrease in  $A_{mix}$  and  $\phi_{mix}$  above the buried gold nanoparticles [see black dots in Fig. 6(d)]. Through detailed numerical analysis of the expected variations in elasticity as well as Rayleigh scattering, the authors concluded that the sample vibration amplitude  $A_s$  must be reduced on the surface directly above the nanoparticles. Note that the expected elasticity contrast, as inferred from Fig. 7(e), for this particular excitation scheme results in an increase of  $A_{mix}$ , opposite to what is measured. As the internal friction of Au is much smaller than

polymers, the friction must happen at their interface. The estimated dissipation of 2.79 eV/oscillation agrees well reported atomic scale friction experiments. Similar work by Sharahi *et al.*<sup>35</sup> performed their experiments with a  $f_{mix} = 200$  kHz, hence much closer to the first contact resonance of the cantilever. Interestingly, the variations in sample elasticity were identified as the main source of contrast in these experiments.

Let us now turn to an example utilizing UFM. Recently, van Es *et al.* published work<sup>86</sup> employing UFM in which the low-frequency  $f_{mix}$  of the amplitude modulation was set equal to the first contact resonance  $f_{res}$  of the cantilever [see Fig. 7(f)]. The samples consisted of a 150 nm thick aluminum structures deposited on a silicon substrate. The aluminum structures were buried with

photoresist or  $\text{SiO}_2$  such that the total thickness of the stack was 300 nm. Note that the fabrication was done such that there were no signatures of the buried structures in the topography of the sample. The AFM was operated in the contact mode with a setpoint force in the range from 200 nN to 800 nN with little observable damage to the sample after scanning. By varying  $f_{mix}$  in a small range around  $f_{res}$ , the authors could show that the observed contrasts, both in amplitude and phase, is related to the local elasticity of the sample. A change in local elasticity shifts  $f_{res}$  resulting in a different, measurable response of the cantilever. When tuning  $f_{mix}$  away from  $f_{res}$ , the contrasts disappear.

Apart from the observation of different contrast mechanisms for different excitation schemes, the lateral resolution of the observed contrasts was different. In case of friction at buried interfaces, one should assume that the amplitude reduction obeys a scattering-like behavior. Moreover, as the measurements are in the near-field regime, the lateral size of the contrasts should be of the order of the depth of the buried features. This is exactly what Verbiest *et al.* found: the lateral size of the nanoparticles at the surface showed a significantly larger diameter than the true diameter of the nanoparticles.<sup>39</sup> If the variations in the elasticity of the sample are the cause of the contrasts, this argumentation does not hold. Moreover, the elasticity is a local surface property. Hence, the observed contrasts have a lateral dimension that is roughly equal to the actual size of the buried features. This is exactly what is observed in measurements employing the contact resonance.<sup>86</sup>

In this section, we discussed the missing link between excitation schemes and contrast mechanisms. By making this link, we highlight the importance of tracking driving and mixing frequencies, as well as contact resonances of the cantilever.

## V. APPLICATIONS

A general 3D nano-acoustic imaging technique would have enormous impact on various field of research and industry. In this section, we highlight the most promising applications for such a technique: semiconductor industry, material science, and life sciences.

### A. Semiconductor industry

It has been recognized that traditional 2D transistors following Moore's law will not be sufficient to satisfy rising demands emanating from the need for more performant electronic devices. Recent advances and future expected surges in demands related to wearable electronics and to the Internet of Things (IoT) further underline the need for a new generation of electronic components. As a result, 3D device architectures that allow for higher performance and lower power consumption have been introduced and are expected, in time, to phase out older generations of transistors. Famous examples of the 3D devices are Gate all Around (GAA) Nanowire FETs (successors of FINFETs) and 3D NAND memory [Figs. 8(a) and 8(b)]. Nanowires are stacked on top of each other below several layers of metal and gate while in 3D NAND memory features are positioned within the layered devices, with up to 120 layers today and in the future to be scaled up to 512 layers.

A new challenge accompanies the introduction of 3D structures in the semiconductor industry: existing nanoscale

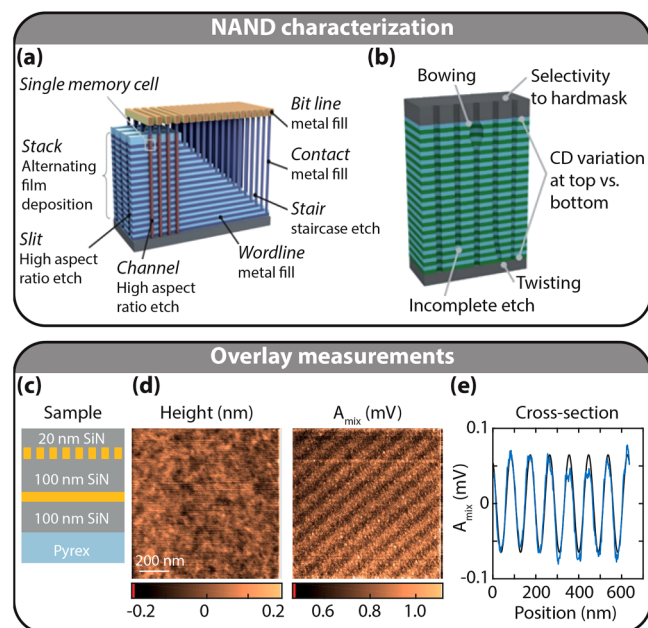


**FIG. 8.** Semiconductor industry in NAND characterization used to (a) check the fabricated devices and to (b) check devices at various fabrications stages. (c)–(e) Overlay measurements as reported by van Es *et al.*<sup>89</sup> (c) Cross section of sample design, (d) height and simultaneously recorded  $A_{mix}$  image, (e) cross section through  $A_{mix}$  image (averaged across all rows of image) with a sine function plotted to show the periodicity and apparent feature size. Panels adapted from Ref. 89.

characterization techniques become insufficient to nondestructively probe the several layers of buried subsurface layers and nanoscale features in the volume of these 3D assemblies. Subsurface AFM imaging has a key role to play in addressing this challenge. In a recent study, Gramse *et al.* presented a new approach,<sup>90</sup> broadband electrostatic force microscopy (EFM), to image of atomically thin dopants n-type (phosphorus) and p-type (boron) buried in silicon. A lateral resolution of 10 nm and depth resolution of 0.5 nm was demonstrated using this technique. Though no subsurface imaging of GAA FETs or 3D NAND has been yet reported, model systems have been used in several studies using acoustic AFM. For instance, heterodyne force microscopy (HFM) has been used to probe the depth of metal-polymer systems,<sup>60,84,91</sup> with a clear application in semiconductor overlay metrology [see Figs. 8(c)–8(e)].<sup>89</sup> Topography images of the nanofabricated samples did not indicate any sign of buried defects, while HFM indicated the presence of voids in the volume of polymer coatings covering silicon nitride.<sup>84</sup> In the case of scanning near-field thickness resonance acoustic microscopy,<sup>60</sup> heterodyne detection was implemented by launching a first wave matching a resonance of the sample and a second wave using the cantilever so that the difference mode synthesized by the tip-sample interaction could be used to sense subsurface features. In this case, tapered holes obtained by focused ion beam (FIB) on silicon (Si) were detected. In addition, sub-100 nm voids in Al/Polymer trench structures could be resolved. Similar studies were

carried out on Cu interconnect patterns.<sup>92</sup> UFM was also used to study systems of interest in the semiconductor industry. UFM images of nanometer-scale mechanical imaging of low-k interconnect test structures revealed the presence of regions with different elasticity as well as a distribution of voids in the Al/polymer system.<sup>93</sup> Furthermore, UFM was used to nondestructively image InAs quantum dots capped with GaAs,<sup>94</sup> AlAs/GaAs superlattices,<sup>94</sup> and InSb/InAs quantum dots superlattice with an approximately 18 nm periodicity capped with a 5 nm InAs layer.<sup>95</sup> Overall, in these studies, the qualitative performance of subsurface AFM in their resolving subsurface defects (voids, sublayer of nanoparticle, etc.) was confirmed. However, as described in previous Sections, at present, the technique is not well controlled so that identifying the depth at which structures and the composition of the feature are buried remains difficult. Nonetheless, the ability to identify the presence of defect below the surface already constitutes a step forward for quality control in the semiconductor industry. Overall the disruption from 2D to 3D semiconductor device architectures will enable a further increase of the performance with the promise of being economically also viable but only if the yield of production is sufficiently high. Acoustic subsurface AFM could provide meaningful feedback to better understand the fabrication and operation of these devices, nondestructively.

## B. Two-dimensional materials

Two-dimensional (2D) materials show distinct properties compared to their bulk counterparts. A large number of 2D materials, including graphene, hexagonal boron nitride, and transition metal dichalcogenides (TMDCs) have triggered a great interest and research, from fundamental investigation to practical applications.<sup>97</sup> The unique properties of 2D materials result from the layered structure, high-surface area, layer-dependent optical bandgap, and variation of chemical compositions.<sup>98</sup> In the aforementioned materials, 2D confinement provides unique mechanical responses, electronic structures, optical characteristics, and electrochemical properties. Electron microscopy and AFM have been extensively used for characterizing these 2D systems but often limiting studies to common modes of AFM.<sup>99</sup> Multi-dimensional and functional characterization under controlled environment is highly sought after to advance the field of 2D material research, for instance, in developments for catalysis and energy.

Ultrasonic-AFM has also been recently implemented for characterization and investigation of 2D materials, particularly, to explore the presence of defects and residues below layers of graphene and molybdenum disulfide ( $\text{MoS}_2$ ).<sup>96</sup> Figure 9 shows some data obtained for a graphite flake (around 50 nm in thickness, excluding folded areas) deposited on a patterned cyclic olefin copolymer (COC) film. Figures 9(a) and 9(b) show the same flake imaged with UFM. The topography [Fig. 9(a)] is identical to the topography acquired by means of the tapping mode-AFM. This shows that minimal damage to the sample surface occurs due to the low friction between the tip and the sample. Moreover, the UFM contrast in Fig. 9(b) clearly shows the contrast from the suspended portions, the latter appearing darker. In Fig. 9(c), the profiles of the lines drawn in Figs. 9(a) and 9(b) are presented. The topographic profile does

not show any major variation that can be attributed to the presence of voids. In the UFM profile, the signal is smaller in correspondence of the voids underneath the flake with a minimum at the center of the suspended areas. This minimum depends on the lateral size of the suspended regions. The UFM signal depends also on the flake thickness. Figure 9(d) shows a second example with a  $\text{MoS}_2$  flake (with thickness varying from 10 to 50 nm) placed on a COC film, patterned with parallel grooves randomly bridged. In this case, the flake is thinner than the graphite flake reported above. The topography signal faintly reveals the presence of grooves underneath, as the flake is less rigid and its shape is affected by the substrate topography. On the other hand, the UFM contrast is even higher than for the case of the graphite flake and still depends on the flake thickness, the lateral size of the suspended regions, and excitation scheme.<sup>100</sup> In another study, UFM was used to probe nanoscale graphene–liquid interfacial interactions.<sup>101</sup> It was shown that effective Young's modulus of graphene reduced slightly in the ambient environment while it reduced by a factor of 3 in the non-polar dodecane environment. Moreover, to understand the atomic nature of the interlayer interaction in graphite, UFM was applied in observing the subsurface edge dislocation within highly oriented pyrolytic graphite (HOPG).<sup>102</sup> It also showed the movement of a dislocation at higher applied forces. This lateral motion demonstrated the considerable sliding between carbon layers, which enables graphite to act as a superior solid lubricant.

## C. Composites

Polymeric nanocomposites, mixtures of polymers with nanofillers (nanoparticles, nanofibers, nanoplatelets, etc.), have been actively developed for automobile, aerospace, electronics, and biomedical industries due to many desirable mechanical, electrical, physical, and chemical properties.<sup>103–105</sup> However, the relationship between internal structures of polymeric nanocomposites (dispersion, orientation, agglomeration, and interface of nanofillers inside polymer matrix) and favorable properties is poorly understood due to the lack of currently available non-invasive, multi-modal nanoscale imaging and characterization techniques. Most manufacturing process variables for polymeric nanocomposites have been determined semi-empirically so far and structure–property relationships in the nanoscale have not yet been firmly established. Recently, AFM was used to characterize the fiber morphology of polymer/clay nanocomposite.<sup>106</sup> Acoustic subsurface AFM techniques are also applied for characterization and visualization of nano-features inside polymeric nanocomposite. In a recent work by Kimura *et al.*,<sup>82</sup> Au nanoparticles deeply buried into the polymer matrix visualized by various ultrasonic-AFM techniques. Figures 10(b) and 10(c) show 2nd-harmonic UAFM images (A and  $\phi$  signals) obtained on a sample with the top-coat thickness of 900 nm of a photo-polymer. These images are compared with the conventional UAFM images [Figs. 10(e) and 10(f)] and HFM images [Figs. 10(h) and 10(i)] on the same area. The sample was actuated at 49 kHz and 98 kHz in 2nd-harmonic UAFM and UAFM, respectively. In HFM, the sample and cantilever were actuated at 800 kHz and 898 kHz, respectively. The results show that all three techniques provided clear images of subsurface gold nanoparticle buried near 1  $\mu\text{m}$  in photopolymer.<sup>82</sup> In another application, epoxy–silica

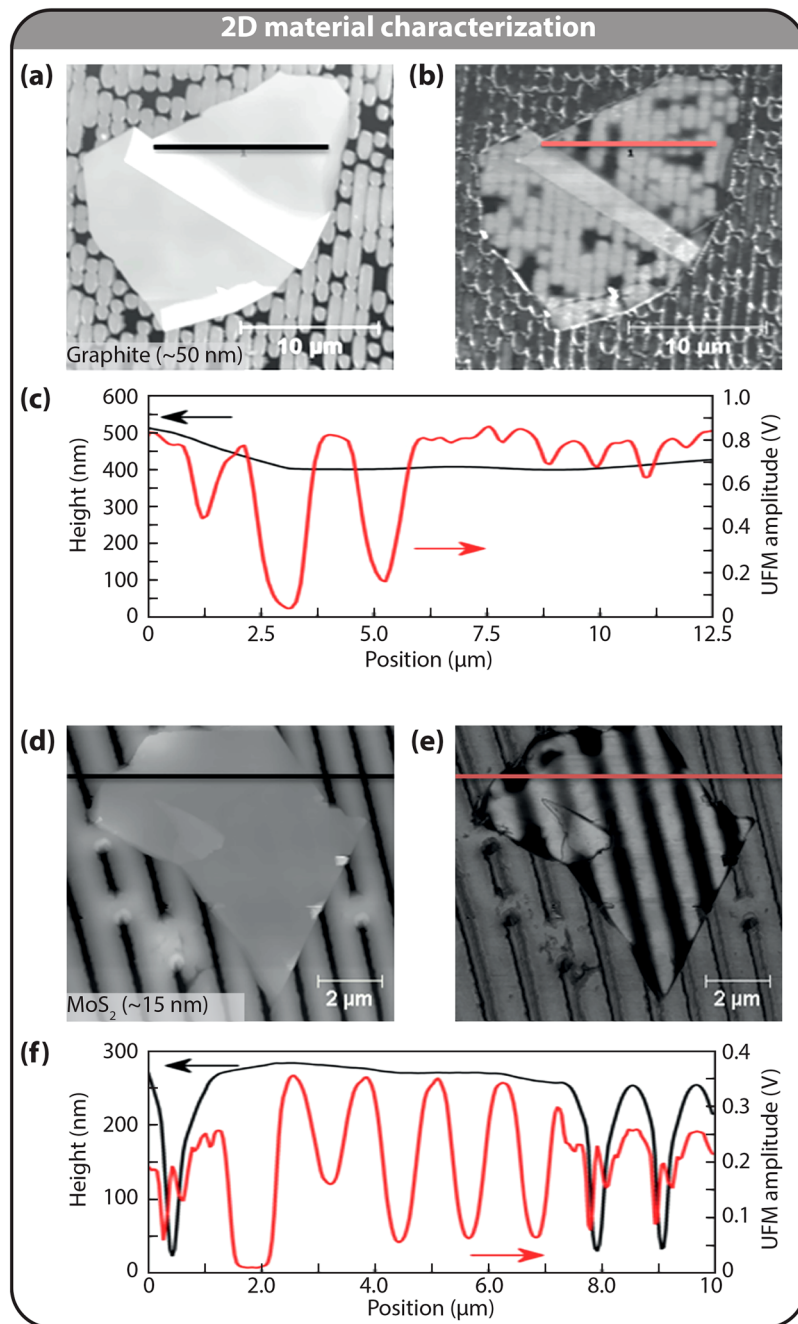


**FIG. 9.** (a)–(c) A graphite flake (around 50 nm thick, excluding folded areas) transferred onto a structured COC film. The UFM image of C<sub>A</sub> (b) clearly shows the regions suspended and not visible in height (a). The darker the UFM contrast, the larger the indentation. (c) Height and UFM profiles of the lines indicated in (a) and (b). (d) Height image of a MoS<sub>2</sub> flake (around 15 nm thick, excluding folded areas) placed on a ridge-structured COC film. (e) UFM image of C<sub>A</sub> shows the areas suspended in dark. (f) Height and UFM profiles of the lines indicated in (d) and (e). Panels have been adapted from Ref. 96.

nanocomposites were examined by AFAM to obtain information about the local elastic modulus of the surface at nanoscale resolution.<sup>107</sup> The capability of AFAM was shown by subsurface imaging of the rigid structure buried under soft matrix such as aluminum under a polymer layer and also rigid structure under rigid matrix such as aluminum under silicon oxide.<sup>86</sup> Additionally, AFAM was applied to visualize the buried nanoparticle in polymer matrix. For

this purpose, silica nanoparticles embedded in different depth into polystyrene matrix. Then, higher contact resonance modes of cantilever were excited to show the effects of buried silica nanoparticle on the contact stiffness between the tip and sample.<sup>32</sup> HFM was also used in nanocomposite applications to reveal the nanoscale elastic and viscoelastic properties of samples of poly(methylmethacrylate) (PMMA)/rubber nanocomposites.<sup>28</sup>

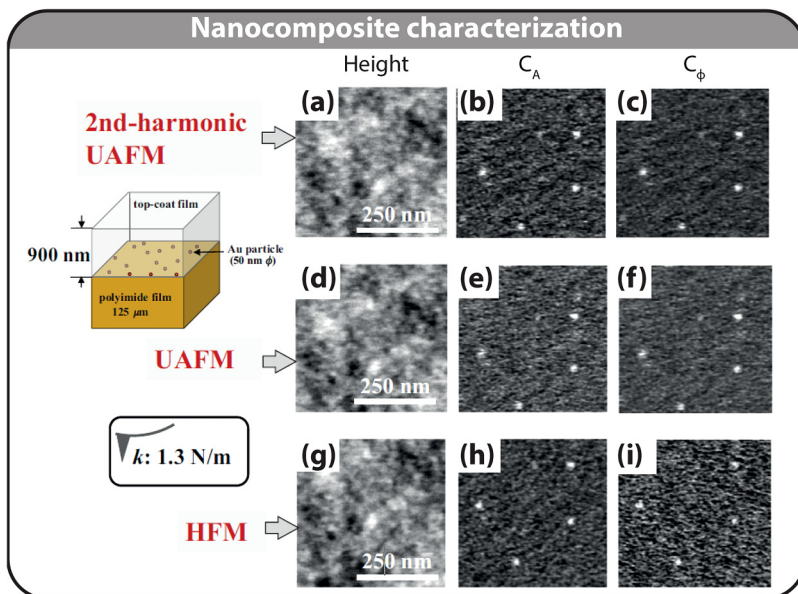


**FIG. 10.** 2nd-harmonic UAFM, UAFM, and HFM images of Au particles buried under the polymer top-coat film (900 nm). The sample was oscillated at 49 kHz and 98 kHz in 2nd-harmonic UAFM and UAFM, respectively. In HFM, the sample and cantilever were oscillated at 800 kHz and 898 kHz, respectively. All the images were obtained by scanning almost the same area. 2nd-harmonic UAFM: (a) height, (b)  $C_A$ , and (c)  $C_\phi$ . UAFM: (d) height, (e)  $C_A$ , and (f)  $C_\phi$ . HFM: (g) height, (h)  $C_A$ , and (i)  $C_\phi$ . The figure is adapted from Ref. 82.

#### D. Life sciences

The versatility of AFM to probe properties of soft matter at the nanoscale, even in a liquid environment, without any requirement of fixation or fluorescent tagging has brought about substantial discoveries in life sciences including, but not limited to, cellular and bio-molecular studies [see Fig. 11(a)]. Other reviews have described the applications of traditional AFM in biological studies from molecular, cellular, and tissue levels comprehensively.<sup>108–111</sup> Here, we highlight the advances reported using nano-acoustic imaging. UFM has shown promising results in visualizing intracellular fibers of live endothelial cells (ECs). The technique is able to reveal an enhancement in stress fibers formation in response to thrombin.<sup>112</sup> HFM, in a form coined scanning near-field ultrasound holography (SNFUH), constituted one of the first attempts to study closed biological systems with nanoscale subsurface imaging. The study demonstrated the ability to detect the presence of malaria parasites within infected red blood cells (RBCs), thereby offering a way to complement histopathological and immunohistochemistry approaches in cases that require sub-100 nm spatial resolution, without the need to disturb the system by chemical treatment or cross-sectioning.<sup>84</sup> A similar technique was used to resolve nanoparticle uptake in macrophages and RBCs collected from mice previously exposed to carbon nanohorns<sup>61</sup> [see Figs. 11(b)–11(g)] and silica nanoparticles<sup>113</sup> inhalation. This study illustrates a field of study where the impact of nanoscale subsurface imaging could be significant as few other tools are available to study the fate and interaction of nanomaterials with complex living systems such as cells and bacteria. Yet, given the surge of nanomaterials used in industrial processes, in pharmaceutical and in antibacterial products for health or agriculture applications, the lack of suitable tools to understand the fundamental interactions of nanoparticles, their evolution in various media such as the human body, plants, water, or cells leaves room for unpredicted long term harmful effects.

The capabilities of HFM were expanded to MSAFM for liquid imaging of cell.<sup>62</sup> The first demonstration of liquid imaging with MSAFM resolved inner structures of keratinocyte skin cells, including their cytoskeleton. Injection of a chemical stressor, pesticide glyphosate, in the liquid medium surrounding the cells led to a significant loss in structure of the cells.<sup>62</sup> Although the capabilities constitute an important instrumental milestone, a number of questions remain when studying complex systems at such scales given the lack of chemical speciation of the technique. For instance, in the proof of concept study of MSAFM,<sup>29</sup> multiple modes were used to image the cell walls of a wood cross section. Although the images provided stark contrast differences, the biological understanding of the plant system did not significantly advance from these findings.

It is generally true that the complexity of changes taking place in biological systems cannot be solely explained from a morphological standpoint. As a result, future efforts focused on combining MSAFM to nanoscale infrared (IR) spectroscopy to gain a deeper understanding of biological systems at the nanoscale. Vitry *et al.* proposed an approach to overlay nanoscale IR maps on top of MSAFM images to determine the composition of the vesicles resolved in bacteria.<sup>114</sup> The findings demonstrate that the chemical signature of lipid corresponds exactly to the location of the round vesicles resolved by MSAFM. In addition to the chemical confirmation, the study performed three-dimensional reconstruction of the inner structure of the bacteria using the MSAFM data. We note that the spatial resolution of the MSAFM images was higher than that chemical mapping. Hence another study considered the combination of MSAFM and chemical imaging to study plant cell walls<sup>18</sup> and showed it was possible to differentiate a cellulose-rich region from a lignin-rich region.

Cells and tissues are inherently heterogeneous material, and visualizing their spatial distribution in mechanical properties is essential for understanding underlying mechanotransduction

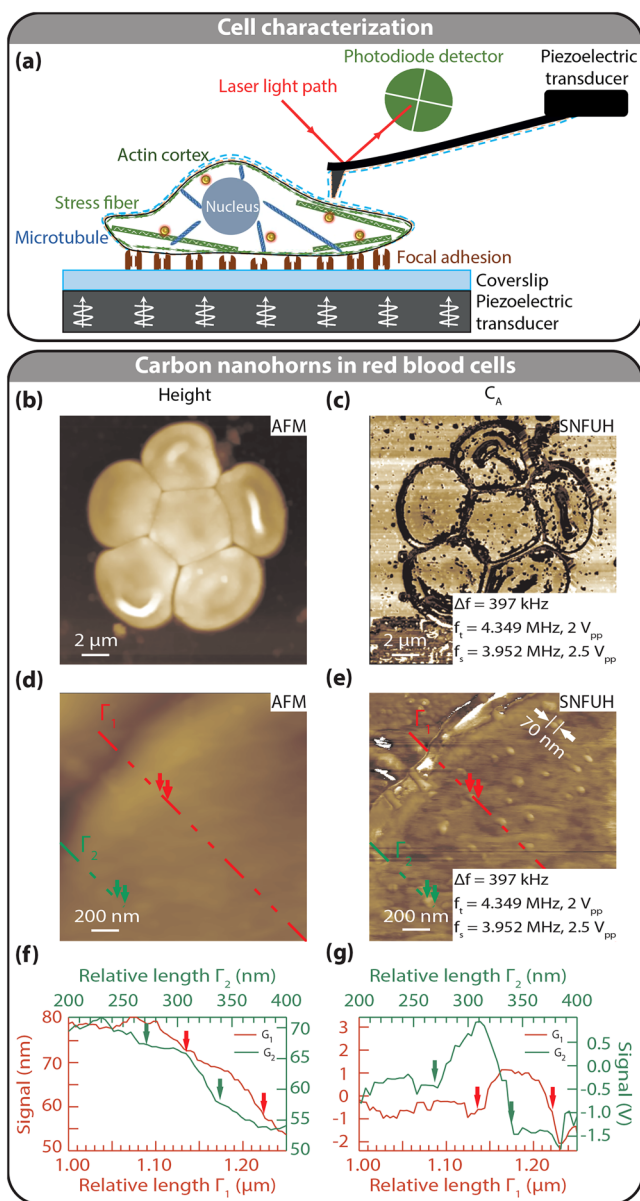


**FIG. 11.** (a) Schematic illustration of a life cell in an acoustic subsurface AFM measurement. (b)–(g) Red blood cells (RBCs) containing carbon nanohorns. AFM height images (b) and (d) and CA images (c) and (e) of carbon nanohorns in RBCs at different scales. Panels (f) and (g) show profiles taken along  $\Gamma_1$  and  $\Gamma_2$  across nanohorns buried in (d) and (e), respectively, show that HFM can resolve nanoparticles that are inside the cells. The figure has been adapted from Ref. 61.

mechanisms.<sup>115</sup> Conventional nano-indentation techniques can be destructive; each indentation may locally form a sizable dent in the sample,<sup>116,117</sup> which not only reduces spatial resolution but also interferes with normal cellular behaviors in real-time

applications and live cell studies. Therefore, a non-destructive to probe physical properties of cells is still needed. As mentioned earlier, nano-acoustic imaging techniques can provide mechanical characteristics of materials such as contact stiffness<sup>118,119</sup> with minimum invasiveness and loading effect on samples,<sup>117</sup> which can be utilized to study the mechanical properties of cells.

Recently, the 3D cell culture has been rapidly emerging for drug screening and tissue modeling. However, limited types of tools such as confocal microscopy and electrical spectroscopy are available for real-time monitoring of cellular behavior in 3D.<sup>120–123</sup> Nano-acoustic techniques, such as UFM, are more likely able to enhance our understandings of how physicomechanical properties of 3D microenvironments can regulate cellular plasticity and mechanotransduction behavior.<sup>112</sup>

## VI. FUTURE DIRECTION

The acoustic subsurface AFM in its current form faces several technical challenges. First, current piezoelectric excitations are limited to relatively low ultrasound frequencies up to a few GHz. At these frequencies, the ultrasound wavelength is of the order of a micrometer, which limits the potential 3D application of the technique. Second, the piezoelectric excitations suffer from spurious resonances in the system. These spurious resonances are mechanical modes of the AFM as well as of the piezoelectric actuator itself. To overcome these limitations, we foresee the development of acoustic subsurface AFM techniques based on photothermal excitations. Photothermal excitations are known to eliminate spurious resonances and thereby offer cleaner signals.<sup>124,125</sup> The combination of AFM cantilevers with pico- or femtosecond ultrasonics offers in this regard an additional advantage, as the ultrashort laser pulses generate high-frequency acoustic pulses with the potential nanometer spatial size. Therefore, future developments in near-field pico- and femtosecond ultrasonics promise great potential for subsurface AFM applications in realizing nano-acoustic imaging.

We also point out that apart from characterizing 2D materials with acoustic subsurface AFM techniques, suspended 2D materials themselves could have an important role in future subsurface AFM techniques. Suspended 2D materials are highly sensitive to changes in their environment which, in combination with their intrinsically high resonance frequency due to their low mass, opens up new possibilities of detecting high-frequency ultrasound. For this purpose, graphene resonators seem ideal candidates because their typical dimensions allow for the integration into standard AFM cantilevers, and they have been shown to detect ultrasound waves within a substrate.<sup>126</sup> This opens up ways to eliminate the need of the non-linear tip-sample interaction in current acoustic subsurface AFM detection schemes.

The development of nano-acoustic imaging is also held back by well-defined reference samples, as it is difficult to validate a new technique, for instance, for opaque samples, if there is no other technique capable of probing the sample at the same scale. To overcome this problem, we propose the following approach. First, transparent samples with a known interior structure can be used. For example, artificial cells containing metallic nanoparticles with fluorescent tags. This allows for validation measurements with super-resolution microscopy and could pave the way

for nano-acoustic imaging on living cells. Some success was achieved by combining micro-Raman spectroscopy and acoustic subsurface AFM to confirm buried carbon nanohorns inside cells.<sup>61</sup> Second, opaque samples encountered in the semiconductor industry can be fabricated in steps. This allows detailed surface characterization at each step from which the final 3D can be inferred. Alternatively, samples can also be cross sectioned afterward with Focused Ion Beam (FIB). Third, nanocomposite samples with embedded nanoparticles in a polymer could be analyzed using Rutherford back-scattering to estimate the depth distribution of the nanoparticles. These sample strategies are vital for the future development of the subsurface AFM.

Recent work shows that the concept of acoustic subsurface AFM encompasses excitations beyond ultrasound waves, such as AC voltages<sup>127</sup> or modulated light.<sup>18</sup> Using the concept of virtual resonance in MSAFM,<sup>59</sup> IR light with laser pulses matching the difference frequency mode synthesized by mixing of two ultrasonic actuations, nanoscale IR imaging with spatial resolution down to 10 nm was demonstrated on polymeric samples and the technique could be applied to study plant cell walls.<sup>18</sup> This, in turn, could constitute an advantageous approach to circumvent inherent limitations of nanoscale IR imaging and spectroscopy obtained by photothermal actuation as it may provide a means to localize information probed in depth, to differentiate surface from volume features. A different approach would be to combine the recently developed scanning thermal probe techniques<sup>24,128</sup> with acoustic subsurface AFM. As the local thermal conductivity is affected by buried features, this could be used to distinguish between the AFM experimental artifacts and buried subsurface features. These lines of work remain in their infancy. However, we believe that their further development will open up new possibilities to study fundamental processes, e.g., electrical and chemical, at the nanoscale.

## VII. CONCLUSION

In summary, we have shown that nanoscale acoustic imaging techniques are most promising to achieve full 3D resolution at the nanoscale.

From recent trends in microscopy, including super-resolution optical microscopy, femto- and picosecond ultrasonic microscopy, and nanoscale subsurface AFM, it seems that probing the volume of complex systems with nanoscale resolution is in reach. A detailed consideration of the latter showed that different configurations are possible, including sample actuation, tip actuation, or both. The frequency range used for the acoustic waves is of tremendous importance to reach the targeted information on or within the sample. This information is related to contrast generated by wave propagation effects, variations in the tip-sample interaction, and/or friction. We analyzed the debate in the existing literature on which one is dominant and conclude that all different contrast mechanisms contribute *simultaneously* to the experimentally observed contrasts. However, the amount in which they contribute to the contrasts is highly dependent on the choice of ultrasound frequencies and their positioning with respect to the (contact) resonance frequencies of the cantilever. We have argued that setting one of the ultrasound frequencies or their frequency

difference to a contact resonance will make the measurement very sensitive to variations in the elasticity of the sample. Mismatching all the ultrasound frequencies with the contact resonances of the cantilever will increase the sensitivity to friction and wave propagation effects. This new insight highlights that acoustic subsurface AFM experiments can be used to study different properties of a sample by just changing the ultrasound frequencies, thereby enabling fast multi-mode sample characterization. In the near future, we expect the development of different tip-enhanced technologies simultaneously employing micro-Raman, laser pulses, or other nano-scale characterization techniques to correlate the 3D structure of a sample with other properties.

The gained insight into the different contrast mechanisms also indicates a major hurdle in achieving full 3D resolution at the nanoscale. In such a technology, it is desired to extract the depth of particular features from a measured quantity. However, this only seems feasible for high-frequency wave propagation effects. To reach the desired frequency regime, in which the ultrasound wavelength is roughly equal to or smaller than the relevant structures, the integration of femto- and picosecond ultrasonic microscopy techniques in acoustic subsurface AFM seems to be the way forward. The ultrasound pulses in femto- and picosecond ultrasonics are so short that a nanometer depth resolution should be possible. Moreover, these pulses would enable pulse-echo imaging, similar to conventional medical ultrasound imaging. The synergy between these research fields may prove to be crucial for the next big technological advances in nanotechnology.

## ACKNOWLEDGMENTS

H.J.S. and S.K. acknowledge support from the Canada Research Chairs (CRC) program and the Natural Sciences and Engineering Research Council of Canada (NSERC). L.T. acknowledges support by the National Science Foundation under Grant No. 1847830. H.S. thanks the project MADEin4 (Metrology Advances for Digitized Electronic Components and Systems Industry 4.0) that has received funding from the ECSEL JU under Grant Agreement No. 826589. The JU receives support from the European Union's Horizon 2020 research and innovation programme and France, Germany, Austria, Italy, Sweden, the Netherlands, Hungary, Belgium, and Israel. G.J.V. acknowledges support by the Dutch 4TU federation for the Plantenna project.

## DATA AVAILABILITY

Data sharing is not applicable to this article as no new data were created or analyzed in this study.

## REFERENCES

- <sup>1</sup>A. Mikhalchan, A. M. Banas, K. Banas, A. M. Borkowska, M. Nowakowski, M. B. Breese, W. M. Kwiatek, C. Palusziewicz, and T. E. Tay, "Revealing chemical heterogeneity of CNT fiber nanocomposites via nanoscale chemical imaging," *Chem. Mater.* **30**, 1856–1864 (2018).
- <sup>2</sup>A. Castellanos-Gomez, J. Quereda, H. P. van der Meulen, N. Agrait, and G. Rubio-Bollinger, "Spatially resolved optical absorption spectroscopy of single- and few-layer MoS<sub>2</sub> by hyperspectral imaging," *Nanotechnology* **27**, 115705 (2016).

- <sup>3</sup>M. Delor, H. L. Weaver, Q. Yu, and N. S. Ginsberg, "Imaging material functionality through three-dimensional nanoscale tracking of energy flow," *Nat. Mater.* **19**, 56–62 (2020).
- <sup>4</sup>Y. Zhang, L. K. Schroeder, M. D. Lessard, P. Kidd, J. Chung, Y. Song, L. Benedetti, Y. Li, J. Ries, J. B. Grimm *et al.*, "Nanoscale subcellular architecture revealed by multicolor three-dimensional salvaged fluorescence imaging," *Nat. Methods* **17**, 225–231 (2020).
- <sup>5</sup>R. Garcia, "Nanomechanical mapping of soft materials with the atomic force microscope: Methods, theory and applications," *Chem. Soc. Rev.* **49**, 5850–5884 (2020).
- <sup>6</sup>D. Maresca, A. Lakshmanan, A. Lee-Gosselin, J. M. Melis, Y.-L. Ni, R. W. Bourdeau, D. M. Kochmann, and M. G. Shapiro, "Nonlinear ultrasound imaging of nanoscale acoustic biomolecules," *Appl. Phys. Lett.* **110**, 073704 (2017).
- <sup>7</sup>T. L. Szabo, *Diagnostic Ultrasound Imaging: Inside Out* (Elsevier Academic Press, Waltham, MA, 2014).
- <sup>8</sup>J. E. Van Der Hoeven, E. B. Van Der Wee, D. M. De Winter, M. Hermes, Y. Liu, J. Fokkema, M. Bransen, M. A. Van Huis, H. C. Gerritsen, P. E. De Jongh *et al.*, "Bridging the gap: 3D real-space characterization of colloidal assemblies via FIB-SEM tomography," *Nanoscale* **11**, 5304–5316 (2019).
- <sup>9</sup>C. Stavrakas, G. Delport, A. A. Zhumekenov, M. Anaya, R. Chahbazian, O. M. Bakr, E. S. Barnard, and S. D. Stranks, "Visualizing buried local carrier diffusion in halide perovskite crystals via two-photon microscopy," *ACS Energy Lett.* **5**, 117–123 (2019).
- <sup>10</sup>J. Mertz, *Introduction to Optical Microscopy* (Cambridge University Press, Cambridge, UK, 2019).
- <sup>11</sup>K. Orhan, *Micro-Computed Tomography (Micro-CT) in Medicine and Engineering* (Springer, 2020).
- <sup>12</sup>P. Russo, *Handbook of X-ray Imaging: Physics and Technology* (CRC Press, Boca Raton, FL, 2017).
- <sup>13</sup>J. Holzgrafe, Q. Gu, J. Beitner, D. M. Kara, H. S. Knowles, and M. Atatüre, "Nanoscale NMR spectroscopy using nanodiamond quantum sensors," *Phys. Rev. Appl.* **13**, 044004 (2020).
- <sup>14</sup>S. Bushong and G. Clarke, *Magnetic Resonance Imaging: Physical and Biological Principles* (Elsevier Mosby, St. Louis, MO, 2015).
- <sup>15</sup>J. Mathurin, E. Pancani, A. Deniset-Besseau, K. Kjoller, C. B. Prater, R. Gref, and A. Dazzi, "How to unravel the chemical structure and component localization of individual drug-loaded polymeric nanoparticles by using tapping AFM-IR," *Analyst* **143**, 5940–5949 (2018).
- <sup>16</sup>J.-X. Cheng and X. S. Xie, "Vibrational spectroscopic imaging of living systems: An emerging platform for biology and medicine," *Science* **350**, aaa8870 (2015).
- <sup>17</sup>C. Prater, K. Kjoller, and R. Shetty, "Nanoscale infrared spectroscopy," *Mater. Today* **13**, 56–60 (2010).
- <sup>18</sup>L. Tetard, A. Passian, R. H. Farahi, T. Thundat, and B. H. Davison, "Opto-nanomechanical spectroscopic material characterization," *Nat. Nanotechnol.* **10**, 870–877 (2015).
- <sup>19</sup>Y. M. Sigal, R. Zhou, and X. Zhuang, "Visualizing and discovering cellular structures with super-resolution microscopy," *Science* **361**, 880–887 (2018).
- <sup>20</sup>T. Fukuma and R. Garcia, "Atomic-and molecular-resolution mapping of solid-liquid interfaces by 3D atomic force microscopy," *ACS Nano* **12**, 11785–11797 (2018).
- <sup>21</sup>E. T. Herruzo, H. Asakawa, T. Fukuma, and R. Garcia, "Three-dimensional quantitative force maps in liquid with 10 piconewton, angstrom and sub-minute resolutions," *Nanoscale* **5**, 2678–2685 (2013).
- <sup>22</sup>C. R. Guerrero, P. D. García, and R. Garcia, "Subsurface imaging of cell organelles by force microscopy," *ACS Nano* **13**, 9629–9637 (2019).
- <sup>23</sup>D. Ebeling, B. Eslami, and S. D. J. Solares, "Visualizing the subsurface of soft matter: Simultaneous topographical imaging, depth modulation, and compositional mapping with triple frequency atomic force microscopy," *ACS Nano* **7**, 10387–10396 (2013).
- <sup>24</sup>G. S. Shekhawat, S. Ramachandran, H. Jiryaei Sharahi, S. Sarkar, K. Huijsak, Y. Li, K. Hagglund, S. Kim, G. Aden, A. Chand *et al.*, "Micromachined chip scale thermal sensor for thermal imaging," *ACS Nano* **12**, 1760–1767 (2018).
- <sup>25</sup>O. A. Castañeda-Uribe, R. Reifenberger, A. Raman, and A. Avila, "Depth-sensitive subsurface imaging of polymer nanocomposites using second harmonic kelvin probe force microscopy," *ACS Nano* **9**, 2938–2947 (2015).
- <sup>26</sup>K. Yamanaka, H. Ogiso, and O. Kolosov, "Ultrasonic force microscopy for nanometer resolution subsurface imaging," *Appl. Phys. Lett.* **64**, 178–180 (1994).
- <sup>27</sup>O. Kolosov and K. Yamanaka, "Nonlinear detection of ultrasonic vibrations in an atomic force microscope," *Jpn. J. Appl. Phys.* **32**, L1095 (1993).
- <sup>28</sup>M. T. Cuberes, H. Assender, G. A. D. Briggs, and O. Kolosov, "Heterodyne force microscopy of PMMA/rubber nanocomposites: Nanomapping of viscoelastic response at ultrasonic frequencies," *J. Phys. D Appl. Phys.* **33**, 2347 (2000).
- <sup>29</sup>L. Tetard, A. Passian, and T. Thundat, "New modes for subsurface atomic force microscopy through nanomechanical coupling," *Nat. Nanotechnol.* **5**, 105–109 (2010).
- <sup>30</sup>C. Tinker-Mill, J. Mayes, D. Allsop, and O. V. Kolosov, "Ultrasonic force microscopy for nanomechanical characterization of early and late-stage amyloid- $\beta$  peptide aggregation," *Sci. Rep.* **4**, 4004 (2014).
- <sup>31</sup>L. Tetard, A. Passian, R. H. Farahi, and T. Thundat, "Atomic force microscopy of silica nanoparticles and carbon nanohorns in macrophages and red blood cells," *Ultramicroscopy* **110**, 586–591 (2010).
- <sup>32</sup>J. P. Killgore, J. Y. Kelly, C. M. Stafford, M. J. Fasolka, and D. C. Hurley, "Quantitative subsurface contact resonance force microscopy of model polymer nanocomposites," *Nanotechnology* **22**, 175706 (2011).
- <sup>33</sup>S. Eslami and N. Jalili, "A comprehensive modeling and vibration analysis of AFM microcantilevers subjected to nonlinear tip-sample interaction forces," *Ultramicroscopy* **117**, 31–45 (2012).
- <sup>34</sup>Z. Parlak and F. Levent Degertekin, "Contact stiffness of finite size subsurface defects for atomic force microscopy: Three-dimensional finite element modeling and experimental verification," *J. Appl. Phys.* **103**, 114910 (2008).
- <sup>35</sup>H. J. Sharahi, G. Shekhawat, V. Dravid, S. Park, P. Egberts, and S. Kim, "Contrast mechanisms on nanoscale subsurface imaging in ultrasonic afm: Scattering of ultrasonic waves and contact stiffness of the tip-sample," *Nanoscale* **9**, 2330–2339 (2017).
- <sup>36</sup>G. J. Verbiest, J. Simon, T. Oosterkamp, and M. Rost, "Subsurface atomic force microscopy: Towards a quantitative understanding," *Nanotechnology* **23**, 145704 (2012).
- <sup>37</sup>S. A. Cantrell, J. H. Cantrell, and P. T. Lillehei, "Nanoscale subsurface imaging via resonant difference-frequency atomic force ultrasonic microscopy," *J. Appl. Phys.* **101**, 114324 (2007).
- <sup>38</sup>H. J. Sharahi, P. Egberts, and S. Kim, "Mechanisms of friction reduction of nanoscale sliding contacts achieved through ultrasonic excitation," *Nanotechnology* **30**, 075502 (2018).
- <sup>39</sup>G. Verbiest, T. Oosterkamp, and M. Rost, "Subsurface contrast due to friction in heterodyne force microscopy," *Nanotechnology* **28**, 085704 (2017).
- <sup>40</sup>P. Vitry, E. Bourillot, C. Plassard, Y. Lacroute, L. Tetard, and E. Lesniewska, "Advances in quantitative nanoscale subsurface imaging by mode-synthesizing atomic force microscopy," *Appl. Phys. Lett.* **105**, 053110 (2014).
- <sup>41</sup>C. Quate, "The AFM as a tool for surface imaging," *Surf. Sci.* **299**, 980–995 (1994).
- <sup>42</sup>G. Verbiest and M. Rost, "Beating beats mixing in heterodyne detection schemes," *Nat. Commun.* **6**, 1–5 (2015).
- <sup>43</sup>P. Vitry, E. Bourillot, C. Plassard, Y. Lacroute, E. Calkins, L. Tetard, and E. Lesniewska, "Mode-synthesizing atomic force microscopy for 3D reconstruction of embedded low-density dielectric nanostructures," *Nano Res.* **8**, 2199–2205 (2015).
- <sup>44</sup>P. Ahn, Z. Zhang, C. Sun, and O. Balogun, "Ultrasonic near-field optical microscopy using a plasmonic nanofocusing probe," *J. Appl. Phys.* **113**, 234903 (2013).
- <sup>45</sup>M. Soliman, Y. Ding, and L. Tetard, "Nanoscale subsurface imaging," *J. Phys. Condens. Matter* **29**, 173001 (2017).
- <sup>46</sup>M. T. Cuberes and J. J. Martinez, "Mechanical-diode mode ultrasonic friction force microscopy," *J. Phys. Conf. Ser.* **61**, 224–228 (2007).

- <sup>47</sup>M. T. Cuberes, "Mechanical diode-based ultrasonic atomic force microscopes," in *Applied Scanning Probe Methods XI* (Springer, 2009), pp. 39–71.
- <sup>48</sup>F. Dinelli, M. Castell, D. Ritchie, N. Mason, G. A. D. Briggs, and O. Kolosov, "Mapping surface elastic properties of stiff and compliant materials on the nanoscale using ultrasonic force microscopy," *Philos. Mag. A* **80**, 2299–2323 (2000).
- <sup>49</sup>U. Rabe, "Atomic force acoustic microscopy," in *Applied Scanning Probe Methods II* (Springer, 2006), pp. 37–90.
- <sup>50</sup>N. Meyendorf, G. Y. Baaklini, and B. Michel, "Nondestructive evaluation and reliability of micro-and nanomaterial systems," in *Proceedings of SPIE* (SPIE, 2002), Vol. 4703.
- <sup>51</sup>W. Arnold, A. Caron, S. Hirsekorn, M. Kopycinska-Müller, U. Rabe, and M. Reinstdtler, "Atomic force microscopy at ultrasonic frequencies," in *Fracture Mechanics of Ceramics* (Springer, 2005), pp. 1–11.
- <sup>52</sup>K. L. Johnson and K. L. Johnson, *Contact Mechanics* (Cambridge University Press, 1987).
- <sup>53</sup>G. Verbiest, D. van der Zalm, T. Oosterkamp, and M. Rost, "A subsurface add-on for standard atomic force microscopes," *Rev. Sci. Instrum.* **86**, 033704 (2015).
- <sup>54</sup>G. Verbiest, T. Oosterkamp, and M. Rost, "Cantilever dynamics in heterodyne force microscopy," *Ultramicroscopy* **135**, 113–120 (2013).
- <sup>55</sup>G. Verbiest, T. Oosterkamp, and M. Rost, "Subsurface-AFM: Sensitivity to the heterodyne signal," *Nanotechnology* **24**, 365701 (2013).
- <sup>56</sup>R. Garcia and E. T. Herruzo, "The emergence of multifrequency force microscopy," *Nat. Nanotechnol.* **7**, 217 (2012).
- <sup>57</sup>S. Santos, C.-Y. Lai, T. Olukan, and M. Chiesa, "Multifrequency AFM: From origins to convergence," *Nanoscale* **9**, 5038–5043 (2017).
- <sup>58</sup>D. Platz, E. A. Tholén, D. Pesen, and D. B. Haviland, "Intermodulation atomic force microscopy," *Appl. Phys. Lett.* **92**, 153106 (2008).
- <sup>59</sup>L. Tetard, A. Passian, S. Eslami, N. Jalili, R. Farahi, and T. Thundat, "Virtual resonance and frequency difference generation by van der waals interaction," *Phys. Rev. Lett.* **106**, 180801 (2011).
- <sup>60</sup>G. S. Shekhawat, A. K. Srivastava, V. P. Dravid, and O. Balogun, "Thickness resonance acoustic microscopy for nanomechanical subsurface imaging," *ACS Nano* **11**, 6139–6145 (2017).
- <sup>61</sup>L. Tetard, A. Passian, K. T. Venmar, R. M. Lynch, B. H. Voy, G. Shekhawat, V. P. Dravid, and T. Thundat, "Imaging nanoparticles in cells by nanomechanical holography," *Nat. Nanotechnol.* **3**, 501–505 (2008).
- <sup>62</sup>M. Ewald, L. Tetard, C. Elie-Caille, L. Nicod, A. Passian, E. Bourillot, and E. Lesniewska, "From surface to intracellular non-invasive nanoscale study of living cells impairments," *Nanotechnology* **25**, 295101 (2014).
- <sup>63</sup>P. Babilotte, P. Ruello, D. Mounier, T. Pezeril, G. Vaudel, M. Edely, J.-M. Breteau, V. Gusev, and K. Blary, "Femtosecond laser generation and detection of high-frequency acoustic phonons in gaas semiconductors," *Phys. Rev. B* **81**, 245207 (2010).
- <sup>64</sup>T. Pezeril, C. Klieber, V. Shalagatskyi, G. Vaudel, V. Temnov, O. G. Schmidt, and D. Makarov, "Femtosecond imaging of nonlinear acoustics in gold," *Opt. Express* **22**, 4590–4598 (2014).
- <sup>65</sup>O. Balogun, "Optically detecting acoustic oscillations at the nanoscale: Exploring techniques suitable for studying elastic wave propagation," *IEEE Nanotechnol. Mag.* **13**, 39–54 (2019).
- <sup>66</sup>P. Ahn, Z. Zhang, C. Sun, and O. Balogun, "Optical detection of ultrasound using an apertureless near-field scanning optical microscopy system," *AIP Conf. Proc.* **1511**, 360–366 (2013).
- <sup>67</sup>S. Hu, C. Su, and W. Arnold, "Imaging of subsurface structures using atomic force acoustic microscopy at GHz frequencies," *J. Appl. Phys.* **109**, 084324 (2011).
- <sup>68</sup>C. Ying and R. Truell, "Scattering of a plane longitudinal wave by a spherical obstacle in an isotropically elastic solid," *J. Appl. Phys.* **27**, 1086–1097 (1956).
- <sup>69</sup>Y. Pao and C. C. Mow, "Scattering of plane compressional waves by a spherical obstacle," *J. Appl. Phys.* **34**, 493–499 (1963).
- <sup>70</sup>K. Graff, *Wave Motion in Elastic Solids*, Dover Books on Physics (Dover, New York, NY, 1991).
- <sup>71</sup>J. David and N. Cheeke, *Fundamentals and Applications of Ultrasonic Waves* (CRC Press, Boca Raton, FL, 2002).
- <sup>72</sup>M. van Es, B. Quesson, A. Mohtashami, D. Piras, K. Hatakeyama, L. Fillinger, and P. van Neer, "Scattering contrast in ghz frequency ultrasound subsurface atomic force microscopy for detection of deeply buried features," <https://arxiv.org/abs/2007.01662> (2020).
- <sup>73</sup>P. van Neer, B. Quesson, M. van Es, M. van Riel, K. Hatakeyama, A. Mohtashami, D. Piras, T. Duivenvoorde, M. Lans, and H. Sadeghian, "Optimization of acoustic coupling for bottom actuated scattering based subsurface scanning probe microscopy," *Rev. Sci. Instrum.* **90**, 073705 (2019).
- <sup>74</sup>T. Dehoux, O. Wright, R. Li Voti, and V. Gusev, "Nanoscale mechanical contacts probed with ultrashort acoustic and thermal waves," *Phys. Rev. B* **80**, 235409 (2009).
- <sup>75</sup>Y. Guillet, B. Audoin, M. Ferrié, and S. Ravaine, "All-optical ultrafast spectroscopy of a single nanoparticle-substrate contact," *Phys. Rev. B* **86**, 035456 (2012).
- <sup>76</sup>K.-H. Lin, C.-M. Lai, C.-C. Pan, J.-I. Chyi, J.-W. Shi, S.-Z. Sun, C.-F. Chang, and C.-K. Sun, "Spatial manipulation of nanoacoustic waves with nanoscale spot size," *Nat. Nanotechnol.* **2**, 704–708 (2007).
- <sup>77</sup>H. Hertz, *J. Reine Angew. Math.* **92**, 156 (1881).
- <sup>78</sup>J. E. Jones, "On the determination of molecular fields. II. From the equation of state of gas," *Proc. R. Soc. A* **106**, 463–477 (1924).
- <sup>79</sup>B. V. Derjaguin, V. M. Muller, and Y. P. Toporov, "Effect of contact deformations on the adhesion of particles," *J. Colloid Interface Sci.* **53**, 314–326 (1975).
- <sup>80</sup>K. L. Johnson, K. Kendall, and A. Roberts, "Surface energy and the contact of elastic solids," *Proc. R. Soc. Lond. A* **324**, 301–313 (1971).
- <sup>81</sup>D. Maugis, "Adhesion of spheres: The JKR-DMT transition using a Dugdale model," *J. Colloid Interface Sci.* **150**, 243–269 (1992).
- <sup>82</sup>K. Kimura, K. Kobayashi, K. Masnf tsuhige, and H. Yamada, "Imaging of Au nanoparticles deeply buried in polymer matrix by various atomic force microscopy techniques," *Ultramicroscopy* **133**, 41–49 (2013).
- <sup>83</sup>A. Sarıoglu, A. Atalar, and F. Degertekin, "Modeling the effect of subsurface interface defects on contact stiffness for ultrasonic atomic force microscopy," *Appl. Phys. Lett.* **84**, 5368 (2004).
- <sup>84</sup>G. S. Shekhawat and V. P. Dravid, "Nanoscale imaging of buried structures via scanning near-field ultrasound holography," *Science* **310**, 89–92 (2005).
- <sup>85</sup>D. Piras, P. van Neer, R. Thijssen, and H. Sadeghian, "On the resolution of subsurface atomic force microscopy and its implications for subsurface feature sizing," *Rev. Sci. Instrum.* **91**, 083702 (2020).
- <sup>86</sup>M. H. van Es, A. Mohtashami, R. M. Thijssen, D. Piras, P. L. van Neer, and H. Sadeghian, "Mapping buried nanostructures using subsurface ultrasonic resonance force microscopy," *Ultramicroscopy* **184**, 209–216 (2018).
- <sup>87</sup>G. Verbiest and M. Rost, "Resonance frequencies of AFM cantilevers in contact with a surface," *Ultramicroscopy* **171**, 70–76 (2016).
- <sup>88</sup>J. A. Turner, S. Hirsekorn, U. Rabe, and W. Arnold, "High-frequency response of atomic-force microscope cantilevers," *J. Appl. Phys.* **82**, 966–979 (1997).
- <sup>89</sup>M. H. van Es, A. Mohtashami, D. Piras, and H. Sadeghian, "Image-based overlay and alignment metrology through optically opaque media with subsurface probe microscopy," in *Metrology, Inspection, and Process Control for Microlithography XXXII* (International Society for Optics and Photonics, 2018), Vol. 10585, p. 105850.
- <sup>90</sup>G. Gramse, A. Kolker, T. Skeren, T. Stock, G. Aepli, F. Kienberger, A. Fuhrer, and N. Curson, "Nanoscale imaging of mobile carriers and trapped charges in delta doped silicon p–n junctions," *Nat. Electron.* **3**, 531–538 (2020).
- <sup>91</sup>G. S. Shekhawat, S. Avasthy, A. K. Srivastava, S.-H. Tark, and V. P. Dravid, "Probing buried defects in extreme ultraviolet multilayer blanks using ultrasound holography," *IEEE Trans. Nanotechnol.* **9**, 671–674 (2010).
- <sup>92</sup>G. Shekhawat and V. Dravid, "Seeing the invisible: Scanning near-field ultrasound holography (SNFUH) for high resolution buried imaging and pattern recognition," *Microsc. Microanal.* **13**, 1220 (2007).
- <sup>93</sup>R. Geer, O. Kolosov, G. Briggs, and G. Shekhawat, "Nanometer-scale mechanical imaging of aluminum damascene interconnect structures in a low-dielectric-constant polymer," *J. Appl. Phys.* **91**, 4549–4555 (2002).

- <sup>94</sup>O. Kolosov, F. Dinelli, A. Robson, A. Krier, M. Hayne, V. Fal'ko, and M. Henini, "Nanometre scale 3D nanomechanical imaging of semiconductor structures from few nm to sub-micrometre depths," in *2015 IEEE International Interconnect Technology Conference and 2015 IEEE Materials for Advanced Metallization Conference (IITC/MAM)* (IEEE, 2015), pp. 43–46.
- <sup>95</sup>O. Kolosov, I. Grishin, and R. Jones, "Material sensitive scanning probe microscopy of subsurface semiconductor nanostructures via beam exit Ar ion polishing," *Nanotechnology* **22**, 185702 (2011).
- <sup>96</sup>F. Dinelli, P. Pingue, N. D. Kay, and O. V. Kolosov, "Subsurface imaging of two-dimensional materials at the nanoscale," *Nanotechnology* **28**, 085706 (2017).
- <sup>97</sup>H. Zhang, J. Huang, Y. Wang, R. Liu, X. Huai, J. Jiang, and C. Anfuso, "Atomic force microscopy for two-dimensional materials: A tutorial review," *Opt. Commun.* **406**, 3–17 (2018).
- <sup>98</sup>D. J. Late, A. Bhat, and C. S. Rout, "Fundamentals and properties of 2D materials in general and sensing applications," in *Fundamentals and Sensing Applications of 2D Materials* (Elsevier, 2019), pp. 5–24.
- <sup>99</sup>M. Abdolahad, M. Janmaleki, S. Mohajerzadeh, O. Akhavan, and S. Abbasi, "Polyphenols attached graphene nanosheets for high efficiency NIR mediated photodestruction of cancer cells," *Mater. Sci. Eng. C* **33**, 1498–1505 (2013).
- <sup>100</sup>K. Yip, T. Cui, Y. Sun, and T. Filleter, "Investigating the detection limit of subsurface holes under graphite with atomic force acoustic microscopy," *Nanoscale* **11**, 10961–10967 (2019).
- <sup>101</sup>B. J. Robinson and O. V. Kolosov, "Probing nanoscale graphene–liquid interfacial interactions via ultrasonic force spectroscopy," *Nanoscale* **6**, 10806–10816 (2014).
- <sup>102</sup>T. Tsuji and K. Yamanaka, "Observation by ultrasonic atomic force microscopy of reversible displacement of subsurface dislocations in highly oriented pyrolytic graphite," *Nanotechnology* **12**, 301 (2001).
- <sup>103</sup>Y. Z. Keteklahijani, A. S. Zeraati, F. Sharif, E. P. Roberts, and U. Sundararaj, "In situ chemical polymerization of conducting polymer nanocomposites: Effect of DNA-functionalized carbon nanotubes and nitrogen-doped graphene as catalytic molecular templates," *Chem. Eng. J.* **389**, 124500 (2020).
- <sup>104</sup>Y. Z. Keteklahijani, M. Arjmand, and U. Sundararaj, "Cobalt catalyst grown carbon nanotube/poly (vinylidene fluoride) nanocomposites: Effect of synthesis temperature on morphology, electrical conductivity and electromagnetic interference shielding," *ChemistrySelect* **2**, 10271–10284 (2017).
- <sup>105</sup>D. R. Paul and L. M. Robeson, "Polymer nanotechnology: Nanocomposites," *Polymer* **49**, 3187–3204 (2008).
- <sup>106</sup>Y. Ji, B. Li, S. Ge, J. C. Sokolov, and M. H. Rafailovich, "Structure and nanomechanical characterization of electrospun PS/clay nanocomposite fibers," *Langmuir* **22**, 1321–1328 (2006).
- <sup>107</sup>M. Pregnenella, A. Pegoretti, and C. Migliaresi, "Atomic force acoustic microscopy analysis of epoxy–silica nanocomposites," *Polym. Test.* **25**, 443–451 (2006).
- <sup>108</sup>Y. F. Dufrêne, D. Martínez-Martin, I. Medalsy, D. Alsteens, and D. J. Müller, "Multiparametric imaging of biological systems by force-distance curve-based AFM," *Nat. Methods* **10**, 847–854 (2013).
- <sup>109</sup>P. Hinterdorfer and Y. F. Dufrêne, "Detection and localization of single molecular recognition events using atomic force microscopy," *Nat. Methods* **3**, 347–355 (2006).
- <sup>110</sup>D. J. Müller and Y. F. Dufrêne, "Atomic force microscopy as a multifunctional molecular toolbox in nanobiotechnology," in *Nanoscience And Technology: A Collection of Reviews from Nature Journals* (World Scientific, 2010), pp. 269–277.
- <sup>111</sup>D. J. Müller and Y. F. Dufrêne, "Atomic force microscopy: A nanoscopic window on the cell surface," *Trends Cell Biol.* **21**, 461–469 (2011).
- <sup>112</sup>G. S. Shekhawat, S. M. Dudek, and V. P. Dravid, "Development of ultrasound bioprobe for biological imaging," *Sci. Adv.* **3**, e1701176 (2017).
- <sup>113</sup>L. Tetard, A. Passian, R. M. Lynch, B. H. Voy, G. Shekhawat, V. Dravid, and T. Thundat, "Elastic phase response of silica nanoparticles buried in soft matter," *Appl. Phys. Lett.* **93**, 133113 (2008).
- <sup>114</sup>P. Vitry, R. Rebois, E. Bourillot, A. Deniset-Besseau, M.-J. Virolle, E. Lesniewska, and A. Dazzi, "Combining infrared and mode synthesizing atomic force microscopy: Application to the study of lipid vesicles inside streptomyces bacteria," *Nano Res.* **9**, 1674–1681 (2016).
- <sup>115</sup>J. Chen, "Nanobiomechanics of living cells: A review," *Interface Focus* **4**, 20130055 (2014).
- <sup>116</sup>W. W. Gerberich, D. Kramer, N. Tymiak, A. Volinsky, D. Bahr, and M. Kriese, "Nanoindentation-induced defect-interface interactions: Phenomena, methods and limitations," *Acta Mater.* **47**, 4115–4123 (1999).
- <sup>117</sup>J. H. Kang, T. P. Miettinen, L. Chen, S. Olcum, G. Katsikis, P. S. Doyle, and S. R. Manalis, "Noninvasive monitoring of single-cell mechanics by acoustic scattering," *Nat. Methods* **16**, 263–269 (2019).
- <sup>118</sup>D. Passeri, A. Bettucci, M. Germano, M. Rossi, A. Alippi, A. Fiori, E. Tamburri, S. Orlanducci, M. Terranova, and J. Vlassak, "Local indentation modulus characterization via two contact resonance frequencies atomic force acoustic microscopy," *Microelectron. Eng.* **84**, 490–494 (2007).
- <sup>119</sup>D. Piras and H. Sadeghian, "Analysis of contact stiffness in ultrasound atomic force microscopy: Three-dimensional time-dependent ultrasound modeling," *J. Phys. D: Appl. Phys.* **50**, 235601 (2017).
- <sup>120</sup>O. Chaudhuri, L. Gu, D. Klumpers, M. Darnell, S. A. Bencherif, J. C. Weaver, N. Huebsch, H.-P. Lee, E. Lippens, G. N. Duda *et al.*, "Hydrogels with tunable stress relaxation regulate stem cell fate and activity," *Nat. Mater.* **15**, 326–334 (2016).
- <sup>121</sup>D. Bavli, S. Prill, E. Ezra, G. Levy, M. Cohen, M. Vinken, J. Vanfleteren, M. Jaeger, and Y. Nahmias, "Real-time monitoring of metabolic function in liver-on-chip microdevices tracks the dynamics of mitochondrial dysfunction," *Proc. Natl. Acad. Sci. U.S.A.* **113**, E2231–E2240 (2016).
- <sup>122</sup>T. H. Booij, L. S. Price, and E. H. Danen, "3D cell-based assays for drug screens: Challenges in imaging, image analysis, and high-content analysis," *SLAS Discov.* **24**, 615–627 (2019).
- <sup>123</sup>C. Jensen and Y. Teng, "Is it time to start transitioning from 2D to 3D cell culture?," *Front. Mol. Biosci.* **7**, 33 (2020).
- <sup>124</sup>K. Yip, T. Cui, and T. Filleter, "Enhanced sensitivity of nanoscale subsurface imaging by photothermal excitation in atomic force microscopy," *Rev. Sci. Instrum.* **91**, 063703 (2020).
- <sup>125</sup>M. E. V. Reijzen, M. S. Tamer, M. H. V. Es, M. V. Riel, A. Keyvani, H. Sadeghian, and M. vd Lans, "Improved sub-surface AFM using photothermal actuation," in *Metrology, Inspection, and Process Control for Microlithography XXXIII* (International Society for Optics and Photonics, 2019), Vol. 10959, p. 109590L.
- <sup>126</sup>G. Verbiest, J. Kirchhof, J. Sonntag, M. Goldsche, T. Khodkov, and C. Stampfer, "Detecting ultrasound vibrations with graphene resonators," *Nano Lett.* **18**, 5132–5137 (2018).
- <sup>127</sup>R. Borgani, D. Forchheimer, J. Bergqvist, P.-A. Thorén, O. Inganäs, and D. B. Haviland, "Intermodulation electrostatic force microscopy for imaging surface photo-voltage," *Appl. Phys. Lett.* **105**, 143113 (2014).
- <sup>128</sup>W. P. King, B. Bhatia, J. R. Felts, H. J. Kim, B. Kwon, B. Lee, S. Somnath, and M. Rosenberger, "Heated atomic force microscope cantilevers and their applications," *Ann. Rev. Heat Transfer* **16**, 287–326 (2013).